SANDIA REPORT

SAND2007-7177
Unlimited Release
Printed December 2007

Innovative High Pressure Gas MEM's based Neutron Detector for ICF and Active SNM Detection

G.A. Chandler, S. Martin, R. Renzi and M.S. Derzon

Prepared by
Sandia National Laboratories
Albuquerque, New Mexico 87185 and Livermore, California 94550

Sandia is a multiprogram laboratory operated by Sandia Corporation,
a Lockheed Martin Company, for the United States Department of Energy's
National Nuclear Security Administration under Contract DE-AC04-94AL85000.

Issued by Sandia National Laboratories, operated for the United States Department of Energy by Sandia Corporation.

Available to DOE and DOE contractors from

U.S. Department of Energy
Office of Scientific and Technical Information
P.O. Box 62
Oak Ridge, TN 37831

Telephone: (865) 576-8401
Facsimile: (865) 576-5728
E-Mail: reports@adonis.osti.gov
Online ordering: http://www.osti.gov/bridge

Available to the public from

U.S. Department of Commerce
National Technical Information Service
5285 Port Royal Rd.
Springfield, VA 22161

Telephone: (800) 553-6847
Facsimile: (703) 605-6900
E-Mail: orders@ntis.fedworld.gov
Online order: http://www.ntis.gov/help/ordermethods.asp?loc=7-4-0#online

SAND2007-7177
Unlimited Release
Printed December 2007

Innovative High Pressure Gas MEM's based Neutron Detector for ICF and Active SNM Detection

Gordon A. Chandler
Diagnostics and Target Physics
Sandia National Laboratories
P.O. Box 5800
Albuquerque, New Mexico 87185-MS1196

Shawn B. Martin, Ronald F. Renzi and Mark S. Derzon
Advanced MEMS
Sandia National Laboratories
P.O. Box 5800
Albuquerque, New Mexico 87185-MS17492

Abstract

An innovative helium3 high pressure gas detection system, made possible by utilizing Sandia's expertise in Micro-electrical Mechanical fluidic systems, is proposed which appears to have many beneficial performance characteristics with regards to making these neutron measurements in the high bremsstrahlung and electrical noise environments found in High Energy Density Physics experiments and especially on the very high noise environment generated on the fast pulsed power experiments performed here at Sandia. This same system may dramatically improve active WMD and contraband detection as well when employed with ultrafast (10-50 ns) pulsed neutron sources.

ACKNOWLEDGMENTS

[Sandia National Laboratories is a multiprogram laboratory operated by Sandia Corporation, a Lockheed Martin Company, for the United States Department of Energy under contract DE-AC04-94AL85000.

We wish to acknowledge those who have contributed to this project. This list includes but is not to Ray Leeper, Doug Chinn, Dora Derzon, Paul Galambos, Sita Mani, Dave Myers, Kenneth Peterson, Don Rohr, Carol Sumpter, Tim Turner, David Zanini, and Tom Zipperian of Sandia Sandia as well as the Science of Extreme Environments LDRD committee who supported this work under LDRD #07-0328.

Contents

FIGURES

TABLES

NOMENCLATURE

atm	atmospheres
dB	decibel
DOE	Department of Energy
ICF	Inertial Confinement Fusion
LTCC	Low-temperature Co-Fired Ceramic
NIF	National Ignition Facility
NTOF	Neutron Time-of-Flight
PSI	Pounds per square inch
SNL	Sandia National Laboratories
TOF	Time of flight
WMD	Weapons of mass destruction

1 INTRODUCTION

Neutron detection systems are required to provide critical data for experiments at Sandia National Laboratories as well as the national Inertial Confinement Fusion (ICF) Campaign. Critical measurements required for these detector systems include:

1. Neutron imaging.
2. Neutron time-of-flight measurements (single hit detector mode)
3. Neutron time-of-flight measurements (current mode)
4. Neutron bang-time measurements.

Neutrons generated in ICF systems are formed in nuclear reactions in high temperature Deuterium plasmas or Deuterium and Tritium plasmas. These reactions as seen in Equation 1.1 and Equation 1.2, yield high-energy 2.45 and 14.1 MeV neutrons.

Equation 1.1

$$D + D \rightarrow {}^{3}He(0.82\ MeV) + n(2.45\ MeV)$$

$$D + D \rightarrow T(1.01\ MeV) + p(3.02\ MeV)$$

Equation 1.2

$$D + T \rightarrow {}^{4}He(3.5\ MeV) + n(14.1\ MeV)$$

Present detector systems for these measurements, which include, scintillators coupled to photomultiplier tubes, scintillating fiber arrays, diamond photoconductive detectors and other systems have their limitations with regards to sensitivity, time response, energy resolution, spatial resolution and background rejection.

An innovative ^{3}He high-pressure gas detection system, made possible by utilizing Sandia's expertise in micro-electrical mechanical fluidic systems, is proposed, that appears to have many beneficial performance characteristics with regards to making these neutron measurements in the high bremsstrahlung and electrical noise environments found in high energy density physics experiments and especially on the very high noise environment generated on the fast pulsed power experiments performed at Sandia.

Complementary utilization of this detector technology for Sandia's missions in Non-Proliferation and Homeland Defense Applications is also foreseen and presented. Specifically we add preliminary suggests for active detection, which would couple this style detector with a short-pulsed neutron source, such as that which could be made with a pulsed power driver (e.g. a dense plasma focus). In this work we borrow heavily from and contribute to on-going work on a pixilated ^{3}He-system for thermal neutron detection[1].

2 HELIUM THREE NEUTRON DETECTORS

2.1 Principles of Operation

Helium three neutron detectors systems are primarily based on the inelastic nuclear reaction,

Equation 2.1

$$ {}^{3}_{2}He + {}^{1}_{0}n \rightarrow {}^{3}_{1}H + {}^{1}_{1}P $$

This reaction, which is also indicated by the notation ^{3}He(n,p) reaction, is an exothermic reaction having a positive energy release or Q-value of 0.764 MeV.[2] The kinetic energy of the tritium and proton charge particle reaction products contain both the kinetic energy of the reacting neutron and helium atom, in addition to the rather large 0.764 MeV reaction energy. The detection of these charge particle products is relatively easy and efficient and coupled with the relatively high neutron interaction cross-section, as shown in Figure 1[3], makes this system the bases for a number of sensitive neutron detector schemes. This reaction has no energy threshold and the cross-section is very large at low neutron energies having a thermal neutron cross-section of 5330 barns. For fast neutrons produced in ICF relevant fusion reactions, such as 2.45 MeV neutrons produced in Deuterium on Deuterium ions, or 14.5 MeV neutrons produced in Deuterium on Tritium ions, the ^{3}He(n,p) cross-sections are ~four orders of magnitude lower, 0.75 and 0.13 respectively. Even so, as will be shown, these cross-sections are high enough to make a relatively sensitive and compact detector for ICF applications.

A neutron detector system utilizing this reaction operates by detecting the energetic tritium and proton ion reaction products. This is typically accomplished by measuring the charge produced due to ionization from the reaction products in the helium gas or liquid cell or through detection of the scintillation light produced in these detector volumes. For low energy thermal neutrons, by conservation of energy and momentum, the reaction products are oppositely directed and share the 0.764 MeV reaction energy as follows:

$$ E_p = 0.573 \text{ MeV and } E_{3H} = 0.191 \text{ MeV}^{4} $$

Where the subscript refers to the specific reaction product.

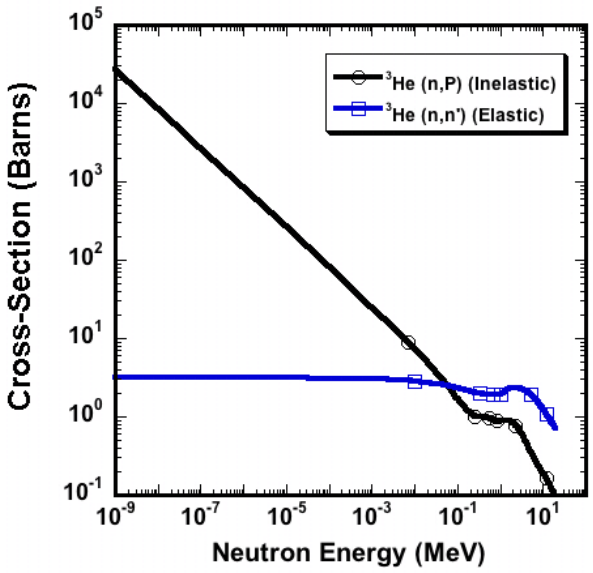

Figure 1. He-3 Neutron interaction cross-sections

For a detector size that is large with respect to the range of the reaction products, the full energy involved with the reaction can be recovered. For a detector that is small with respect to the reaction product range, energy will be lost to the walls, in what is appropriately known as the wall effect. At standard temperature and pressure the range of a 0.573 MeV proton is 5.16 cm and the range of a 0.191 MeV triton is 1.46 cm[5]. The ability to operate the detectors at high densities, either by using high pressures as we propose in our detection scheme and/or by

cooling the gas, allows for smaller volumes to be used while maintaining efficient detection of the reaction products.

The pulse height spectra one might expect to see for low energy neutrons with the wall effect is shown in Figure 2.[6] As can be seen in this figure the peak energy deposited by the reaction products is the full energy peak consistent with the Q-value for the reaction. The plateaus in the pulse height spectrum between 191 and 573 and 573 and 764 keV are due to the sum of observed energy when either the proton or the triton reaction product is separately absorbed into the wall of the detector while the other reaction product is completely observed. Since the reaction products are oppositely projected in the case of 'slow' neutrons, due to the kinematics, this is a highly likely outcome.

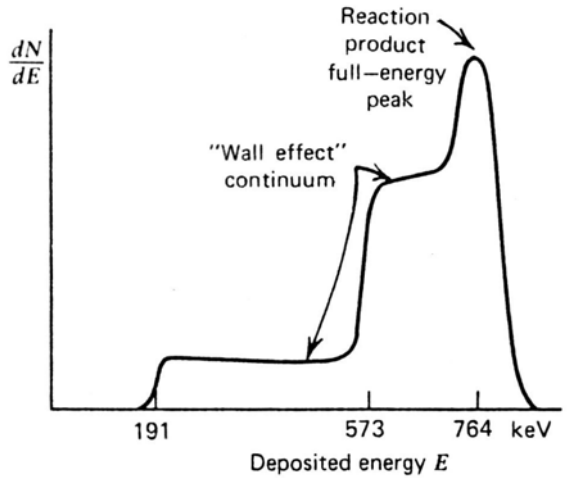

Figure 2. Thermal Neutron pulse height spectrum with wall interactions[5]

In case 1 assume the triton reaction product is absorbed into the wall depositing from 0 to 191 keV of its energy with equal probability. If the remaining, detectable triton energy is added to the energy of the 573 keV proton reaction product then an observable step function in the pulse height spectrum, from 573 to 764 keV is expected. In case 2 assume the proton reaction product is absorbed into the wall depositing from 0 to 573 keV of its energy with equal probability. If the remaining detectable proton energy is added to the energy of the 191 keV triton then an observable step function in the pulse height spectrum from 191 to 764 keV is expected. Summing the probability of these two cases along with a number of full energy events yields qualitatively the spectrum as shown in Figure 2. Detailed modeling of the wall effect for cylindrical ^{3}He counters for thermal neutrons is given by Shalev et. Al[5]. In real systems structure can be found in the pulse height spectra due elastic scattering off ^{3}He and thermal neutron absorption as well. For simplicity these features are not shown in figure 2 but will be discussed further below.

In a pulse counting mode where one would like to discriminate against other background signatures, such as high-energy bremsstrahlung, the wall interactions reduce the number of events that can be observed if the event thresholds need to be set above the minimum 191 keV values and hence reduces the detection sensitivity. In a current detection mode the broad spectrum complicates the mapping of charge collected to the number of neutrons incident on the detector.

As described in Knoll's book, 'Radiation and Detection Measurement', a number of detectors have been based on this reaction scheme. For slow, <0.5 eV neutron detection, these include ^{3}He proportional counters, ionization chambers, and spectrometers. A plethora of other detectors, including scintillators, activation detectors, and bubble chambers have also been used as neutron diagnostics.

For fast, high energy, neutron detection, as required for ICF applications, two effects in the ^{3}He reaction cross-sections, as shown in Figure 1, are important. One is that the inelastic scattering cross-section is falling

rapidly with neutron energy, from greater then 10^4 barns at thermal energies, to only 0.75 barns at 2.45 MeV and 0.13 barns at 14 MeV. Thus a detection scheme based on directly observing the fast neutrons by this reaction will have to discriminate against any unwanted low energy neutrons produced in the experiment, such as from source neutrons scattered off materials in the experimental geometry. The second effect seen in the cross-section plot is the relatively large elastic scattering cross-section at high energies. Elastic scattering dominates the interactions above neutron energies greater then 60 keV. At 2.45 MeV the elastic scattering cross-section is 2.3 barns, or about 3x larger then the inelastic cross-section and at 14 MeV the elastic scattering cross-section is 0.94 barns or about 7.2 times larger then the inelastic cross-section. Thus the neutron energy deposition in the ^{3}He detector begins to be dominated by the elastic reactions. A third reaction channel opens up for fast neutrons with an energy greater then ~5 MeV. The ^{3}He(n,D) reaction channel, as seen in Figure 3[7], opens up and has a cross-section ~50% less then the ^{3}He(n,p) reaction. The Q-value for this endothermic reaction is -3.27 MeV[8].

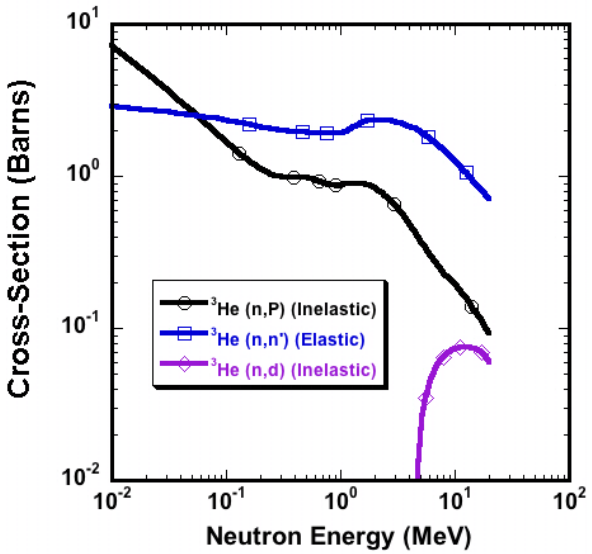

Figure 3. ^{3}He Neutron Interaction Cross Sections

In light of these properties a class of ^{3}He detectors used for neutron dose and yield measurements use a moderator to thermalize the fast neutrons and then count them based on the large thermal reaction cross-section[9,10,11].

For direct fast neutron detection in a ^{3}He detector a differential energy spectrum for a monochromatic neutron with an energy greater then 0.764 MeV incident on the detector, without the effects of wall losses, is expected to have a shape as given by Knoll[12] and is reproduced in Figure 4. As explained by Knoll the energy spectrum consists of three features. A full energy peak generated by the inelastic reaction channel and given by the energy of the incident neutron, E_n, plus the 0.764 MeV reaction Q-value. The second feature is the ^{3}He recoil peak generated by the elastic collision of the neutron with the ^{3}He and which is limited by the kinematics to a maximum value of ¾ of the neutron energy. The third feature is the Epithermal peak. This peak is due to the inelastic reaction with source neutrons that are thermalized in the detector and laboratory environment. Reaction product interactions with the walls of the detector, for reaction product ranges larger then the active volume of the detector, will smear out these peaks to lower energy.

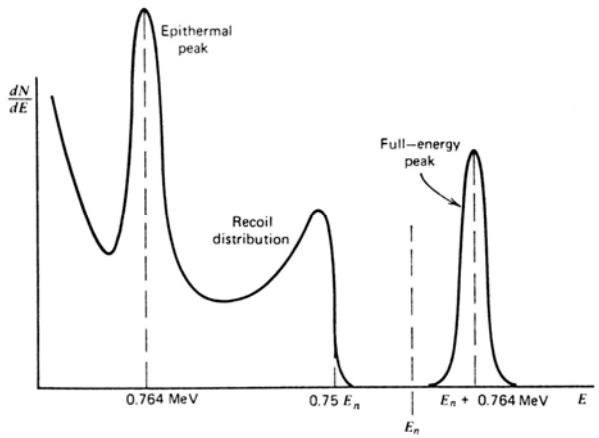

Figure 4. Fast Neutron pulse height spectrum without wall interactions[11]

To maximize the energy deposited in a fixed volume of detector one wants to maximize the number of ^{3}He atoms and reduce the range of the reaction products by also maximizing the number of ^{3}He atoms and by possibly doping the active volume with higher Z gases such as krypton. However using higher Z gases to reduce the range of the reaction products will increase the sensitivity of the detector to high-energy bremsstrahlung radiation.

^{3}He detectors are relatively insensitive to bremsstrahlung radiation for a number of reasons. For one the photon interaction cross-sections due to Photoelectron, Compton and Pair production mechanisms, which deposit energy into electrons and hence into the gas detection medium are relatively small for a low Z gas such as ^{3}He. The Photoelectric interaction cross-section scales approximately as Z^5, the Compton scattering cross-section scales with the number of electrons and hence as Z, and the pair-production cross-section scales roughly as Z^2.[13] As seen in Figure 5 the incoherent, Compton scattering, cross-section dominates the photon absorption, in a primary energy range of interest, from 10 keV up to 50 MeV. where the cross-section ranges from ~1 barn to ~0.03 barns[14]. Typical shielding for fast neutrons will filter out lower energy photons. These cross-sections are comparable to the nuclear interaction cross-sections shown in Figure 3. However the energy deposition into the active detection region containing the ^{3}He gas due to these photoelectrons is or can be made to be less then for the elastic or inelastic nuclear reactions.

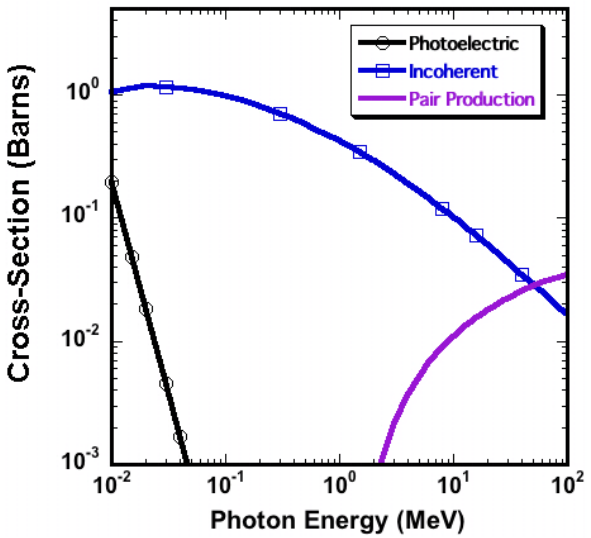

Figure 5. Helium photon scattering cross-section

This is due to both the positive Q-value for the ^{3}He(n,P) reaction and due to the relatively long range of the electrons in the ^{3}He gas medium compared with the reaction products from the nuclear interactions. This can be seen in Figure 6, showing the ranges of the nuclear reaction products consisting of protons, tritons, and elastically scattered ^{3}He ions[15] as well as photoelectrons[16] in microns verse the particle energy in MeV. These ranges were calculated for ^{3}He gas at a pressure of 1000 atm and at 20°C. Using the ideal gas law this yields a mass density of 0.125 g/cc and an ion density of 2.5×10^{22}. As seen in this plot the electron ranges are one to two orders of magnitude larger then the range for an equivalent nuclear reaction product. Thus the electrons can be made to range out of a gas volume that will contain the nuclear reaction products and hence deposit significantly less energy then the equivalent energy ion. Note at this gas density the range of MeV reaction products are less then 100 microns. As will be seen later using a better high-pressure equation of state for helium, at 3000 atm (the upper limit we anticipate using for these capillary arrays) the density of helium at room temperature is approximately

the same as the ideal gas value used here. However at 3000 atm and liquid nitrogen temperatures it is over 2 times the ideal gas value used here and hence the reaction product range would be over 50% smaller. This short range allows for efficient collection of the energy deposited in glass with the small diameter capillaries we envision using.

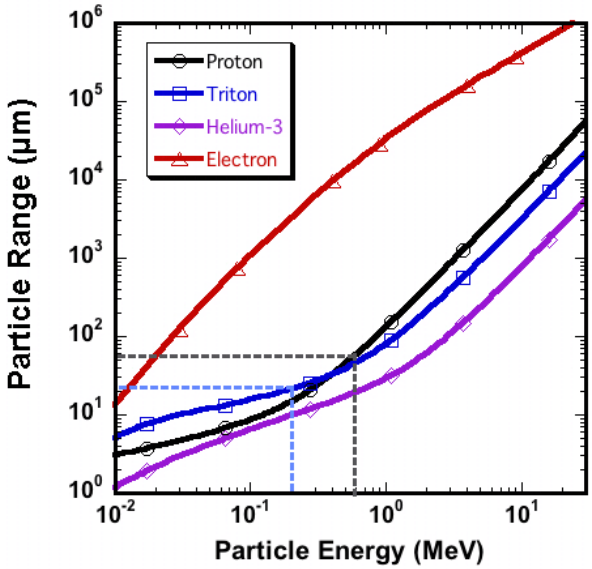

Figure 6. Reaction Product Ranges in 1000 atm ^{3}He at 20°C

Another interaction with the background bremsstrahlung radiation is direct photonuclear interactions. At photon energies in the 5 to 30 MeV range these have been measured for ^{3}He and include the ^{3}He(γ,p)d and the ^{3}He(γ,pp)n reactions.[17] As can be seen in Figure 7, presented in Shima's paper, the total photonuclear absorption cross-section peaks at ~15 MeV at ~2 mb, ~1000 times less than the nuclear interaction cross-sections

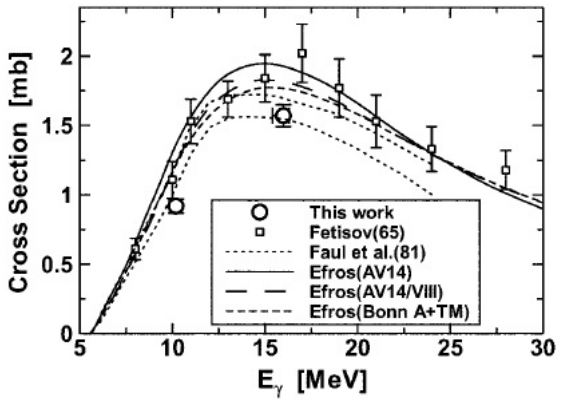

Figure 7. Total ^{3}He photonuclear absorption cross-section

In practice a ^{3}He spherical dose equivalent neutron detector has demonstrated a neutron/gamma ratio better than 1000:1 for a range of gamma energies from 0 to at least 7 MeV.[9]

The intent of this LDRD is to maximize the advantages afforded by the ^{3}He detector for high neutron to gamma sensitivity by integrating it into a compact and robust detection system afforded by high-pressure capillary array systems.

2.2 Helium-4 vs Helium-3 detector characteristics

In light of the large role that the elastic cross-section plays in the response of the ^{3}He detector system at ICF relevant neutron energies, ~1 – 20 MeV, it is interesting to compare the response of a ^{4}He detector to that of the ^{3}He detector. A neutron interacting with ^{4}He at these energies deposits it's energy only through an elastic scattering interaction. As can be seen in Figure 8 the ^{4}He elastic neutron scattering cross-section is actually higher then the ^{3}He cross-sections starting at a neutron energy of ~0.6 MeV. The ^{4}He cross-section peaks at 1.1 MeV, where it is ~4x larger than the ^{3}He elastic cross-section. At 2.5 MeV the ^{4}He elastic cross-section is ~40% larger then

larger then the ^{3}He cross-section and at 14 MeV they are about equal with the ^{4}He cross-section being ~7.4% higher then the ^{3}He cross-section.

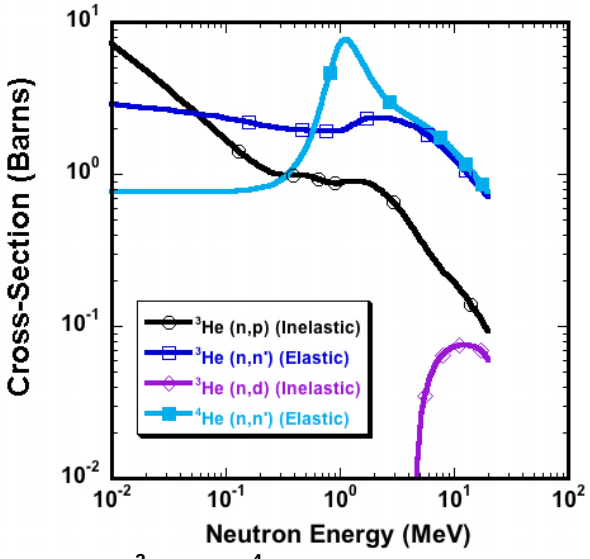

Figure 8. ^{3}He and ^{4}He Neutron interaction cross-sections

The actual response of the detectors will be related to the energy deposited in the detectors due to the neutron interactions. In Table 1 we show the results of a calculation of the average energy deposition due to a single neutron interaction. In this calculation we assume that the average energy deposition in the elastic reactions are half the maximum kinetic energy that can be given to the target nucleus from the neutron. As can be seen in this table for a 2.5 MeV neutron the average energy deposited in a ^{3}He verse ^{4}He detector is ~ a factor of two higher. For a 14 MeV neutron the energy deposition into a ^{3}He vs ^{4}He detector is a factor of 50% higher. So if one wants to get the maximum detectable signal and/or if one wants to use thresholding in a photon counting configuration to discriminate against background noise sources, i.e. relying on the inelastic neutron reaction, then it appears as if using ^{3}He may be warranted. In a current mode detector system it appears that if you can live with the reduced sensitivity of a ^{4}He detector then the nontrivial expense of obtaining ^{3}He (~$140/liter) can be avoided. In addition the neutron interaction cross-section at low energy for ^{4}He is a fairly constant ¾ of barn for neutron energies from epithermal energies all the way up to ~0.1 MeV. This actually allows for much better low energy neutron discrimination compared with ^{3}He, which has a huge inelastic cross-section at lower energies. These low energy neutrons would primarily come from scattering events in the experimental geometry, and would be isolated from the desired fast neutron signal based on their delayed detector arrival times.

Neutron Energy (MeV):	2.5	2.5	14	14
Target atom:	^{3}He	^{4}He	^{3}He	^{4}He
Maximum Elastic Energy Transfer Fraction:	0.75	0.64	0.75	0.64
Elastic Cross-Section (barns):	2.4	3.18	0.94	1.06
Inelastic Cross-Section (barns):	0.75	0.00	0.14	0.00
Total Cross-Section (barn):	3.15	3.18	1.08	1.06
Q-Value (MeV):	0.76	0.00	0.76	0.0
Elastic Reaction Average Energy Deposition (MeV):	0.94	0.80	5.25	4.48
Inelastic Reaction Average Energy Deposition (MeV):	3.26	0.00	14.76	0.00
Average Total Reaction Energy Deposited (MeV):	**1.5**	**0.8**	**6.5**	**4.48**

Table 1. ^{3}He and ^{4}He Neutron Energy Deposition for DD and DT fusion neutrons

This result opens up the possibility of using other gases that have high elastic cross-sections compared with helium. Naturally one might consider that a hydrogen or deuterium gas would possibly fill this role. As seen in Figure 9 however, showing the total neutron interaction cross-sections for hydrogen, deuterium, ^{3}He and ^{4}He, for DD and DT neutron energies at 2.45 and 14 MeV, as indicated by the vertical lines on the plot, the helium cross-sections are actually higher then the hydrogen and deuterium cross-sections.

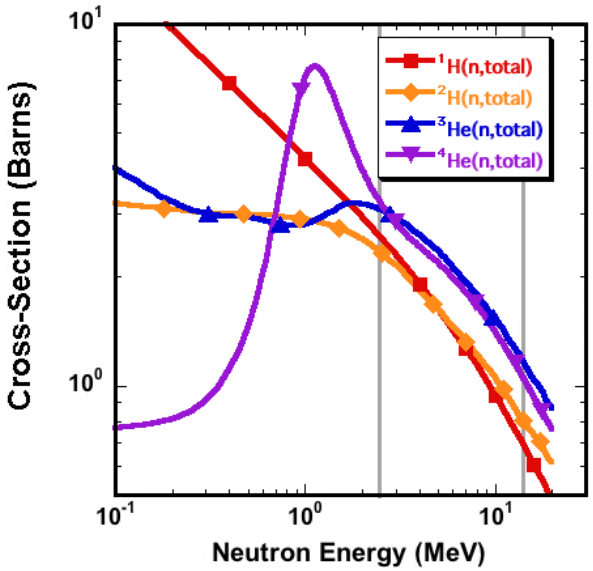

Figure 9. Total neutron interaction cross-sections for Hydrogen, Deuterium, ^{3}He and ^{4}He

2.3 Proton Recoil Scintillator Detector Comparisons

2.3.1 Proton Recoil Scintillator Detectors

Proton recoil scintillator detector systems are a standard detector system for detecting fast neutrons in ICF applications. They have been used for NTOF in both current mode[18] and single hit detector mode[19] as well as for neutron imaging[20] and neutron bang and burn-width measurements[21]. In order to elucidate the comparative analysis between these standard detector systems and a ^{3}He detector system we need to look at the properties of these detectors.

Proton recoil scintillator detectors convert the incident neutron energy into recoil protons, which excite and ionize the scintillator material. A fraction of the energy deposited is emitted as prompt fluorescence or scintillation photons typically with photon energies in the near UV to the blue region of the visible spectrum (~350-450 nm). In ICF applications organic plastic scintillators with relative fast, ~1-2 ns decay times; such as Saint-Gobain's BC-418, BC-422 and BC-436 (a deuteriated plastic scintilaltor) are usually used. In addition to the prompt fluorescence with a few ns decay time and relatively slow delayed fluorescence components with time responses of tens and hundreds of ns are usually observed.[22] This can be an issue in some ICF applications when trying to observe a delayed neutron signal from the source with a small amplitude compared with the prompt neutron signal from the source, for instance when looking at down-scattered neutrons.

2.3.2 Cross-Section and Signal Comparisons

The neutron interaction cross-sections for plastic scintillators are determined by its constituents, which are primarily Hydrogen and Carbon in approximately a 1:1 atomic ratio. Figure 10 shows the elastic and inelastic neutron interaction cross-sections for Hydrogen, Carbon and ^{3}He. As seen in this figure the dominant cross-sections are the elastic cross-sections with all of them ~1.5-2.5 barns for a 2.5 MeV DD neutron and 0.7-0.8 barns for a 14 MeV DT neutron. The inelastic scattering cross-section for ^{3}He is 0.7 barns and 0.13 barns for a 2.5 MeV and a 14 MeV neutron respectively. The two inelastic neutron interaction cross-sections on carbon, the ^{12}C(n, α)^{9}Be (Q-value: -5.7 MeV) and the ^{12}C(n, n+2α)α (Q-value: -7.3 MeV), have energy thresholds of 6.17 MeV and 7.98 MeV respectively.

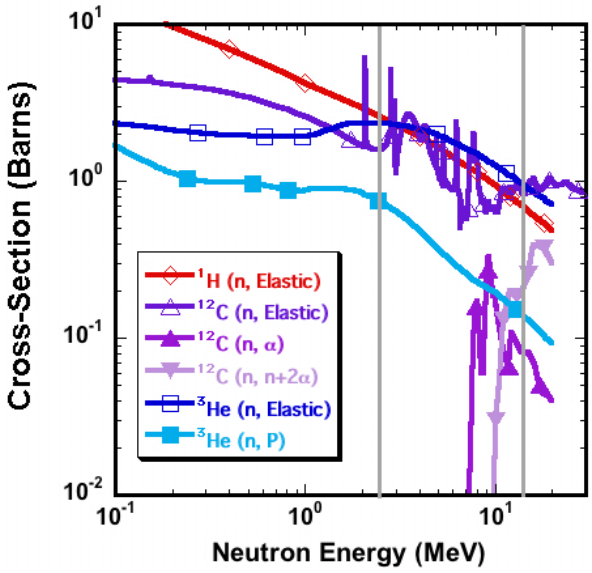

Figure 10. Neutron interaction cross-sections for plastic scintillators and ^{3}He[23]

Since one figure of merit of the detector system is the energy deposited by the neutrons we will now look at the energy deposition into the scintillator and compare it with the energy deposition into a ^{3}He detector. The total interaction probability, $P_t(\varepsilon)$, for a monochromatic neutron interacting with a detector can be given as:

Equation 2.2

$$P_t(\varepsilon) = n\sigma_t(\varepsilon)L = nL\sum_i \sigma_i(\varepsilon) = \sum_i P_i(\varepsilon)$$

where n is the atomic number density, $\sigma_t(\varepsilon)$ is the total interaction cross-section as a function of energy, $\sigma_i(\varepsilon)$ is the individual interaction cross-section, L is the length of the detector in the direction of motion for the neutron and $P_i(\varepsilon)$ is the interaction probability for a given type of interaction i. The average energy deposited per interaction, E_{ave}, is then given as:

Equation 2.3

$$P_t(\varepsilon)E_{ave} = \sum_i P_i(\varepsilon) * E_{i\_ave}$$

Yielding,

Equation 2.4

$$E_{ave} = \frac{1}{\sigma_t(\varepsilon)}\sum_i E_{i\_ave}\sigma_i(\varepsilon)$$

Where E_{i_ave} is the average energy deposited for a given type of interaction i.

The neutron interaction with the hydrogen in the scintillator is purely due to the elastic scattering of the neutron off the proton. In this interaction the kinematics allows for the neutron to deposit up to its full energy into the proton. The energy distribution function of proton recoils due to monochromatic neutron interactions turns out to be a step function out to the full neutron energy. Hence the average energy deposited for a single neutron interaction is half the incoming neutron energy. For the elastic scattering of the neutron off of the carbon nuclei the maximum energy transfer is 28.4% of the incoming neutron. However the light generated in a plastic scintillator is very dependant on the specific ionization of the particle and, as can be seen in Figure 11, is significantly less for a carbon particle compared with a proton. Therefore we will ignore the contribution of the energy deposition due to the neutron induced carbon interactions in the scintillator. As shown in Figure 12 this leads to neutron interaction mean-free paths with the protons in the plastic scintillator that for DD and DT neutrons are comparable to that for helium at 2000 atm and room temperature, i.e. ~10 and 40 cm respectively. For helium at liquid nitrogen temperatures the neutron interaction mean-free paths are smaller for helium then for hydrogen in the plastic scintillators, i.e. ~7 and 20 cm respectively. This decrease in the mean-free path for 14 MeV neutrons can make a significant difference in the signal to noise ratio in situations where the scintillators are limited in thickness, such as in neutron imaging. For example at 2000 atm and at 77°k for a 5 cm thick detector a 20% improvement

in the signal to noise is possible based on the increase in the number of interactions.

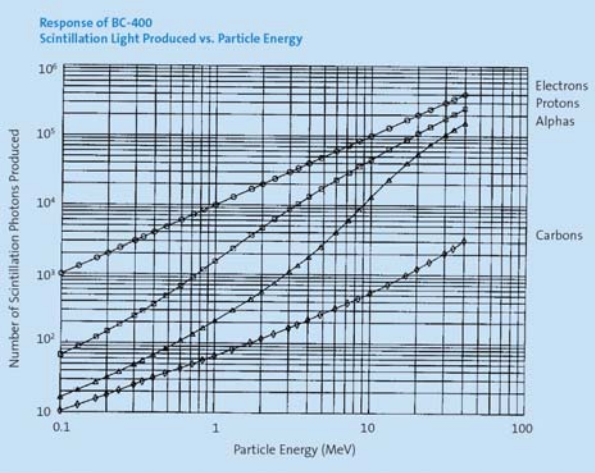

Figure 11. Scintillation light produced vs. Particle and Particle energy[24]

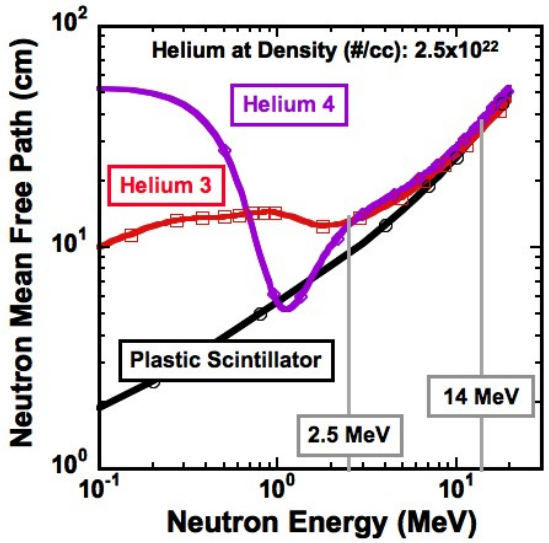

Figure 12. Neutron interaction mean-free path vs Neutron Energy

For ^{3}He for the elastic scattering contribution we will assume we also have approximately a step function distribution in energy with the maximum energy given to the ^{3}He atom limited by kinematics to 75% of the incoming neutron energy. Thus the average energy imparted to the ^{3}He atom is:

Equation 2.5

$$E_{He3\_elastic\_ave} = \frac{0.75E_n}{2}$$

In Figure 13 the average energy deposited for ^{3}He, ^{4}He and the hydrogen in plastic scintillator is shown. For fast 2.5 and 14 MeV neutrons the energy deposition is similar for ^{3}He and hydrogen and they are both ~50% higher in the average energy deposition compared with ^{4}He. Note that the average energy deposited in the ^{3}He gas per collision is less then the positive Q-value of 0.76 MeV due to the inclusion of the lower energy elastic reaction channel.

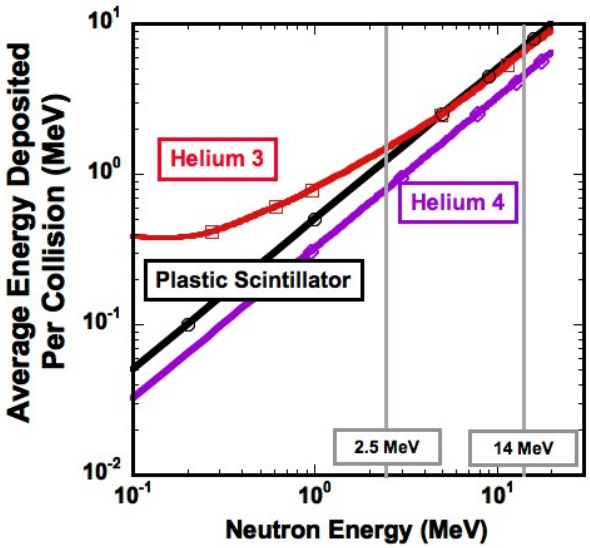

Figure 13. Average energy deposited per collision for the Hydrogen in plastic scintillators and ^{3}He and ^{4}He

In Table 2 we compare the average energy deposited per neutron collision between ^{1}H and ^{3}He for 2.5 MeV DD neutrons and 14 MeV DT neutrons. As seen in this table the average energy deposition, assuming the reaction products are all contained within the detector volume, are very comparable between the two atoms.

Neutron Energy (MeV):	2.5	2.5	14	14
Target atom:	^{3}He	^{1}H	^{3}He	^{1}H
Maximum Elastic Energy Transfer Fraction:	0.75	1	0.75	1
Elastic Cross-Section (barns):	2.4	2.6	0.94	0.69
Inelastic Cross-Section (barns):	0.75	0.00	0.14	0.00
Total Cross-Section (barn):	3.15	2.6	1.08	0.69
Q-Value (MeV):	0.76	0.00	0.76	0.0
Elastic Reaction Average Energy Deposition (MeV):	0.94	1.25	5.25	7.00
Inelastic Reaction Average Energy Deposition (MeV):	3.26	0.00	14.76	0.00
Average Total Reaction Energy Deposited (MeV):	**1.5**	**1.2**	**6.5**	**7.0**
Energy/Scintillation photon-Ws (eV/hv):	300	750	300	300
# of Scintillation Photons:	**5000**	**1600**	**22000**	**23000**
Number Density n_t*10^{-22} (#/cc):	2.5	4.2	2.5	4.2
Interaction Length (cm):	12.7	9.2	37.0	34.8
Relative Energy Deposited per unit volume:	1.00	1.15	1.00	1.15
Relative # of Scintillation Photons per unit volume:	2.2	1	0.9	1
1 MeV Photon Interaction Fraction, 10 cm long	0.1	0.5	0.1	0.5
Relative # of Scin. Photons/1 MeV Photon Interaction	11	1	4.5	1
Relative # of Scintillation Photons per unit volume For Xenon doped 3He	22	1	9	1
1 MeV Photon Interaction Fraction: Xe doped, 10 cm long	0.18	0.5	0.18	0.5
Relative # of Scin. Photons/1 MeV Photon Interaction, Xe doped	62	1	25	1

Table 2. ^{3}He and ^{1}H Energy Deposition and Scintillation properties

The energy required per scintillation photon, W_s, is also given in Table 2. The value for ^{3}He was obtained from data given by Birk[25] while the value for hydrogen was based the sensitivity of BC-422, which was obtained from the data given in Saint-Gobain Crystals literature for the plastic scintilator BC-400 and it's relative response to BC-422[26]. Thus the average number of scintillation photons per interaction, as seen in Table 2, is ~3 times higher for ^{3}He then for BC-422 (as given in the ^{1}H column) for 2.5 MeV DD neutrons and at 14 MeV both of the medium have similar photon yields. Our estimate for the number of scintillation photons produced by 14 MeV neutrons in plastic scintillators, 23000, is comparable to the value of 20700 estimated by Ress[27] as well as that given by Disdier[28] for organic liquid scintillators of 13200.

However the scintillation efficiency for ^{3}He detectors can be improved significantly with the utilization of a small amount of Xenon. With only a 3% atomic doping of Xenon the W_s value was observed to be only 34 eV/photon.[29] This would increase the light yield from a pure ^{3}He gas scintillator counter by ~9 times yielding an enhancement over the plastic scintiallator of ~20 times for a 2.5 MeV neutron and ~9 times for a 14 MeV neutron. The tradeoff would be enhanced bremsstrahlung sensitivity in the ^{3}He detector doped with Xenon.

To compare the two detection media with regards to the average energy deposition per unit volume in the material we can express the energy deposited in a given medium as:

Equation 2.6

$$E_d = E_{ave} N_c = E_{ave} N_n (1 - \exp(n_t \sigma_t L))$$

which is approximately equal to:

Equation 2.7

$$E_d \approx E_{ave} N_n n_t \sigma_t L$$

where, N_n is the number of neutrons incident on the detector, n_t is the number density of target atoms and σ_t is the total interaction cross-section. Note that the interaction length in the detector medium, l_i, is given by

Equation 2.8

$$l_i = \frac{1}{(\sigma_t n_t)}$$

For ^{3}He if we take a number density of $2.5x10^{22}$ consistent with a room temperature, i.e. 20°C, high-pressure cell at ~2000 atm, as seen in Figure 20, then the interaction length is ~13 cm for a 2.5 MeV neutron and 37 cm for a 14 MeV neutron. As seen in Table 2, this is similar to that for the Hydrogen in the plastic scintillator whose chemical formula is $H_{11}C_{10}$ and having a density of 1.032 gm/cc. This indicates that the detector volumes for both systems will be essentially equal to intercept a given number of neutrons. The relative energy deposited per unit volume in the two detector mediums as calculated from Equation 2.7 is given in Table 2. As can be seen in this table the plastic scintillator has a 15% higher energy deposition as compared with the ^{3}He and the relative number of photons generated per unit volume in ^{3}He is two times higher at 2.5 MeV and ~10% less at 14 MeV as compared with a plastic scintillator. If Xenon can be doped into the gas, i.e. the bremsstrahlung background is not too high, then the light output at both neutron energies can be a factor of 10 to 20 times higher!

The number of signal carries generated in a 5 cm long detector per incident neutron can be seen in Figure 14.

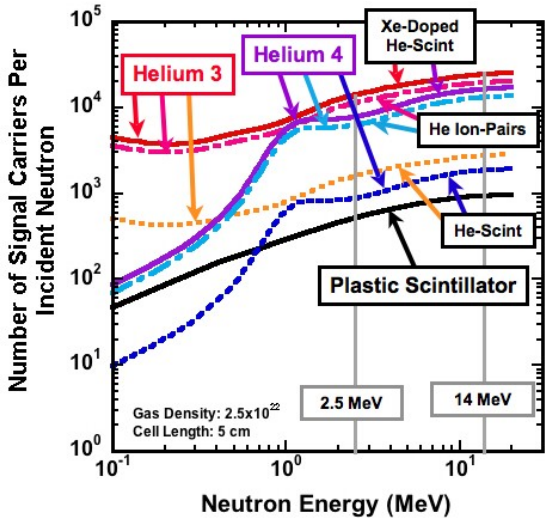

Figure 14. The number of signal carriers, i.e. Scintillation photons or Ion-pairs for Helium and Xenon-doped Helium gas compared with Plastic Scintillator

In this figure we plot in addition to the scintillation photons generated in the plastic scintillator and the Helium gas, both doped and undoped, we also plot the ion-pairs formed taking the energy/ion-pair as 42.3 eV as given by Birks.[30] Note that the undoped Helium gas scintillator yields ~2-3 times the number of photons as the plastic scintillator in the range of neutron energies from ~1-20 MeV while the Xenon doped scintillator yields over an order of magnitude greater scintillation photons over this range of energies as compared with plastic scintillator. If one can collect the electron-ion pairs formed then the doped or undoped Helium gas cells can be used to yield over an order of magnitude higher signal in this energy range as compared with plastic scintillators.

As discussed above the generation of signal carriers in the detector volumes by fast neutrons in helium detectors compared to plastic scintillators can be over an order of magnitude higher. If these secondary signal carriers could be collected with equivalent efficiencies to the plastic scintillators then the signal to noise of a detection system under Poisson statistics for the observed signal of

interest is developed in Appendix A and is given by:

Equation 2.9

$$\left(\frac{S}{N}\right)_{No} = \frac{N_s N_n}{\sqrt{FN_n^2 N_s + N_s^2 N_n}} = \frac{\sqrt{N_s N_n}}{\sqrt{FN_n + N_s}}$$

Where, N_n is the number of interacting neutrons in the detector, N_s is the number of signal carriers generated per neutron and F is the Fano factor. According to Knoll, the Fano factor is significant only in single counting mode, not in current mode data collection as would be typical in our ICF applications and so we can set it's value to 1.[31] As can be seen from this equation, if the number of incident neutrons is low compared with the number of signal carriers generated per neutron then the signal to noise in the detected signal just goes as the square root of the number of interacting neutrons. If on the other hand the number of interacting neutrons is high compared to the number of signal carriers generated per neutron then the signal to noise in the detected signal goes as the square root of the number of signal carriers generated per neutron and we would have gained up to a factor of three improvement in the signal to noise for our high pressure Helium detector. As can be seen in Figure 14, the number of signal carriers per MeV neutron is ~300-1000 for plastic scintillator and for our Helium detector it is ~8000-10000. For a typical neutron imaging application the number of neutrons incident on a detector pixel element is expected to be up to a few thousand where the neutron counting statistics puts the S/N at ~50. Figure 15 shows the improvement in the signal to noise for a Helium detector that yields 10 times the number of signal carriers per neutron as a plastic scintillator for four different signal carrier yields as a function of the number of interacting neutrons. As can be seen from this plot if the number of interacting neutrons is small, a few hundred for instance, the improvement with the number of signal carriers is small. For the case of a few thousand interacting neutrons, the improvement in the signal to noise can be expected to be ~1.5 to 2 times with the larger number of signal carriers available in the Helium detector. If the ICF based neutron diagnostic could be operated in this regime a significant improvement in the S/N could be obtained.

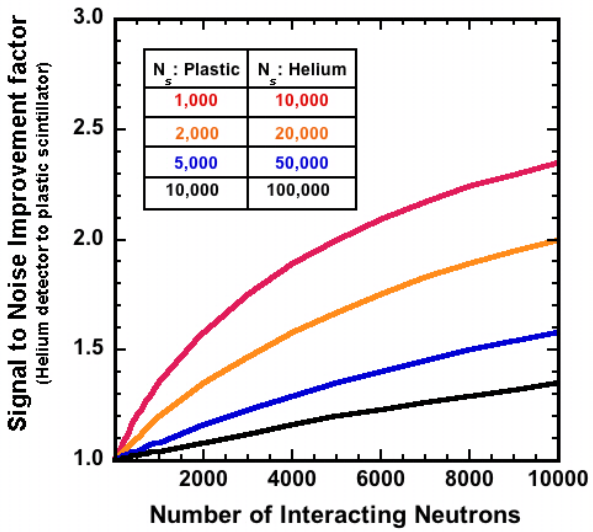

Figure 15. The signal to noise improvement factor comparing a Helium detector to a plastic scintillator

In addition to potential improvement in the signal to noise for the Helium detector over the scintillator with the larger number of signal carriers, there is also the potential improvement in the ability to observe the source. In typical ICF neutron imaging applications the scintillating-fiber detector collection efficiencies are not very high. The fiber optic collection efficiencies in the fibers are typically 2-5%, the collection optics which transport the photons to a gated image intensifier which have been used are 0.5% for an F/# 2.72 optical collection system and 4% for a fiber-optically coupled system. The quantum efficiency of an image intensifier is typical ~10-20%. Thus the overall efficiency in generating photon electrons in the image intensifier per scintillation photon generated

can be only $1x10^{-5} – 4x10^{-4}$. If enough scintillator photons are not generated in the fibers, 2500 – 100000, then the ability to count single neutrons incident on the detector is severely limited and the signal to noise will be poor. This was the case for 2.5 MeV neutron detection presented in L. Disdier paper.[32] Thus the much larger number of signal carriers created in the Helium gas cell, if they can be collected, (see section 2.6) can significantly improve the flexibility in the overall diagnostic configuration with the potential for improved signal sensitivity and signal to noise characteristics.

2.3.3 Bremsstrahlung Sensitivity Comparisons

Another figure of merit comparing the helium detectors to plastic scintillator detectors is to look at their relative sensitivity to bremsstrahlung radiation. To get an estimate of the sensitivity of the two mediums to bremsstrahlung radiation we will compare the total photon interaction cross-section. As seen in Figure 16, the photon mass-absorption cross-section for plastic scintillator, and a Helium gas cell above ~40 keV is fairly similar. The Xenon doped gas cell in a range between 0.4 and 6.0 MeV is also fairly similar and so the photon interaction in a detector filtered to see photons only above ~400 keV, ~1 cm of Tungsten, will respond primarily according to the mass density of the material.

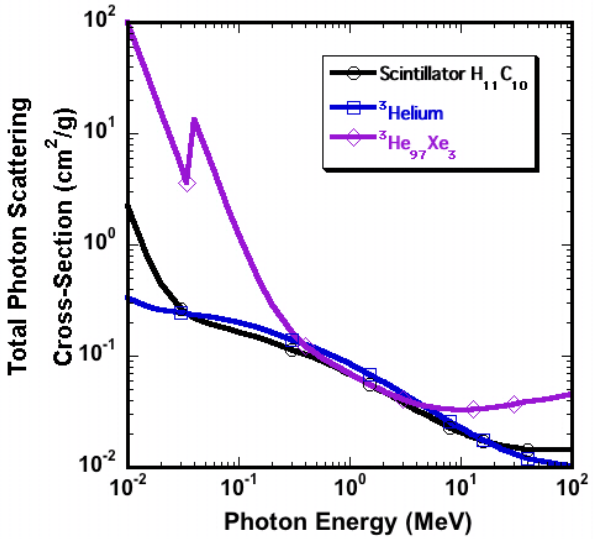

Figure 16. The mass absorption cross-section for plastic scintillator, ^{3}He and Xenon doped ^{3}He[33]

For a plastic scintillator the mass density is typically 1.1 gm/cc and for the ^{3}He detector at ~2000 atm the mass density is ~0.125 mg/cc. For a ^{3}He gas cell doped with Xenon at 3% atomic such that the ^{3}He number density is the same as that of a pure ^{3}He detector, the mass density would be 0.288 gm/cc. Figure 17 shows the number of photons that would interact in a 10 cm long detector for the different detector materials based on the mass absorption cross-sections presented. As can be seen in this plot over a range of photon energies from ~400 keV to 10 MeV the ^{3}He detector has ~ 3 to seven times less interactions as compared with the plastic scintillator. Over this range in photon energies even the Xenon doped ^{3}He gas cell has ~ a two times lower interaction probability. Thus if a figure of merit is defined as the light output divided by the photon interaction probability for a detector 10 cm long then, as can be seen in Table 2, the ^{3}He detectors figure of merit is 10 to 20 times higher then for the plastic scintillator for 14 and 2.5 MeV neutrons respectively, and the Xenon doped ^{3}He detector is 25 to 60 times better then the plastic scintillator for this figure of merit! The actual improvement will depend on a more

accurate calculation that we will base on Monte-Carlo neutron and radiation transport modeling, but the potential for a significant improvement looks promising.

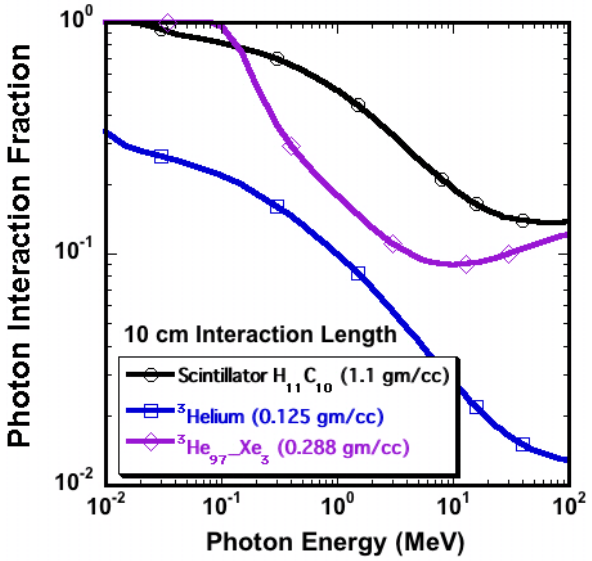

Figure 17. Photon Interaction fraction for plastic scintillator, ^{3}He and Xenon doped ^{3}He

In fact this figure of merit should also include the range of the photo-induced electrons as they ultimately deposit the energy from the photons into the material. As given by Robley[16], the electron range is directly related to the material density. Thus the ^{3}He detector is expected to have an electron range that is eight times longer then the range in a plastic scintillator. As seen in Figure 6, one MeV electrons travel ~1 cm in the Helium gas cell. For a plastic scintillator the range would therefore be ~1.25 mm. For detectors that are large with respect to these dimensions one might expect the observed backgrounds to be equivalent between the scintillator and gas detectors. However two effects will favor the Helium gas detector.

One is due to the electron vs proton recoil efficiency in generating fluorescence. As seen in Figure 11 the number of scintillation photons for a plastic scintillator for electrons at a given energy is significantly greater then that produced by expected recoil protons. Gas detectors, as reported by Birks[34], 'have the notable feature …. 'that the scintillation response is practically proportional to the particle energy dissipated in the scintillator over a very wide range of dE/dr'. Thus the signal to background for a given gamma or hard bremsstrahlung background will be worse in a plastic scintillator as compared with a gas scintillator, perhaps by an order of magnitude given the data in Figure 11.

The other effect favoring our conceived high-pressure helium detector is that it will be fabricated from capillary array structures made from a glass material with capillary diameters on the order of a few hundred microns. Thus a large fraction of the photoelectrons generated will range out of the gas and into the glass substrate. In principal this could be done for the organic scintillator also, but then the ratio of the effective range difference for electrons between the two materials of a factor of eight, would favor the gas scintillator.

2.3.4 Spatial Resolution Comparisons

The range of the reaction products limits the spatial resolution of the scintillating fiber arrays. This is also true for the gas detector. To get a sense for the relative resolution determined by the range of elastically scattered protons in scintillator verses alphas in Helium gas or Helium gas doped with 2% Xenon we plot the range of these particles based on the SRIM code calculations[35] in Figure 18. As can be seen in this figure, above ~1 MeV the range for the ^{4}He (or alphas), is ~two times less then for the protons in the plastic scintillator. In these calculations we used a ^{4}He gas density consistent with Helium at 2000 atm and at 20°C. Since the Mean energy for elastic scattering 14 MeV neutrons off the protons in the plastic scintillator is 7

MeV whereas for ^{4}He this value is ~5 MeV, due to the recoil kinematics. The conclusion to be drawn is that one might estimate that approximately a factor of four improvement in the spatial resolution of a Helium detector over a plastic scintillator detector is possible. Note further improvements are possible by cooling the gas down to liquid nitrogen temperatures where the density can be enhanced by ~50%. Note also that actual spatial resolution limits based on the particle ranges depend on detailed modeling. Monte-Carlo calculations by Disdier et. al. indicate that for a liquid scintillator entrained in a glass capillary array the spatial resolution was limited to ~750 um in a standard liquid organic scintillator and ~500 um in a deuterated liquid organic scintillator[36]. These detector spatial resolutions require high magnification systems (~50) on ICF facilities to achieve the desired 10 um source resolutions. A helium detector system with a spatial resolution improvement of 2-4 times would make a significant improvement in the performance of an ICF neutron imaging system.

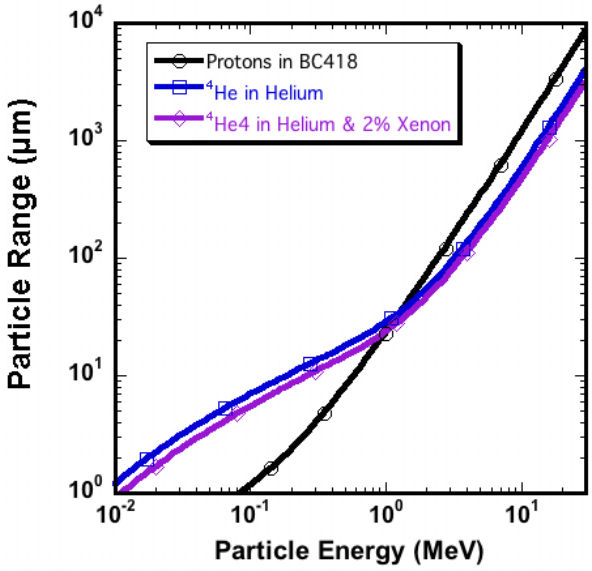

Figure 18. Particle ranges vs Particle Energy for Protons in BC418 Plastic Scintillator and ^{4}He in Helium gas (180 mg/cc) and Helium gas with 2% Xenon by number (297 mg/cc)

2.4 ^{3}He Equation of State

In order to minimize the physical size of the detector and to optimize it's spatial resolution we are interested to maximize the atomic number density of the ^{3}He gas. In order to do this, the gas can be pressurized and/or cooled. The ^{3}He equation of state represents the number density verse the applied temperature and pressure of the system. As will be discussed later, glass capillaries have been tested up to ~3000 atm of pressure and presently this represents an upper range to the pressures we envision for these detectors. At standard pressure ^{3}He liquefies at 3.191 °K. The critical point properties for 3He are: T_c 3.324 (°K); P_c 1.15 (atm) and a critical density of 0.0413 g/cc[37], yielding a critical point number density of 8.29×10^{21} atoms/cc. Above the critical point the phase boundary between the gas and liquid state ceases to exist and only a solid / supercritical fluid phase boundary is observed. This boundary was measured for ^{3}He by Grilly and Mills from ~30 atm to 3440 atm and is shown in Figure 19[38]. As can be seen in this figure for pressures up to 3000 atmospheres the temperature required to get to the solid/supercritical fluid boundary is ~30°K, yielding a fluid number density of $\sim 5.5 \times 10^{22}$ atoms/cc. If we operate at higher temperatures, from perhaps liquid nitrogen temperatures at 77°k to room temperature, for ease of diagnostic fielding, then one can see that we will be in the supercritical fluid state and that the number density, for pressures below 3000 atmospheres will be less then 5.5×10^{22} atoms/cc.

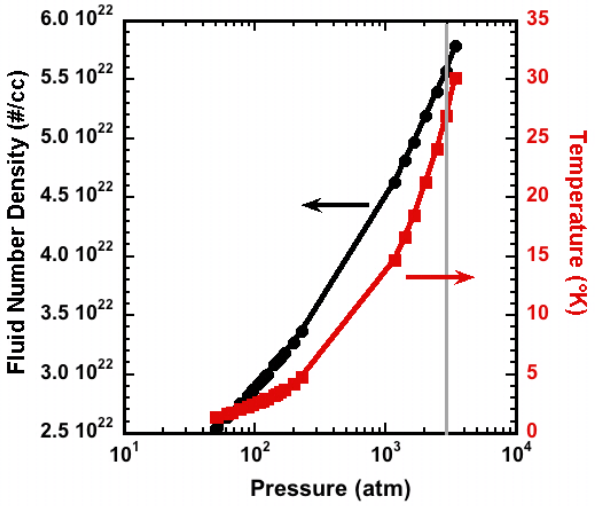

Figure 19. Helium 3 Melt Boundary Plot

The equation of state for ^{3}He in this temperature and density range is far from the range where the quantum mechanical effects distinguishing the behaviors of fermion-like ^{3}He and boson-like ^{4}He would be evident and so the expected density vs pressure curves should be equivalent. Never the less the density verse pressure curve, as seen in Figure 20, is far from ideal. This figure shows a plot of density verses pressure for ^{3}He at room temperature (293°k) and at liquid nitrogen temperature (77°k) for an ideal gas and for an equation of state derived from a fit to ^{4}He data by Mills[39]. Mills, et. al. derived an equation of state from fits to ^{4}He data from 75 to 300 °k and for pressures from ~2000 to 20000 atmospheres. The fits were extrapolated to lower pressure after verifying a good correlation to the ^{4}He compressibility data given by Cramer[40] taken at 298°k and for pressures between 100 – 1400 atm. As can be seen in this plot helium starts to behave non-ideally above ~200 atm and the number density at 3000 atm appears to be limited to ~3.4×10^{22} (0.17 g/cc) for 293°k and ~5.1×10^{22} (0.26 g/cc) for 77°k. Note that as shown in Figure 20 at 3000 atm the helium number density is actually larger then the number density of hydrogen in plastic scintillators.

Increasing the pressures above 3000 atm yields only a marginal improvement in the gas density. Note that the number density of liquid Helium at 4° K and 1 atm pressure is 2.0×10^{22} atoms/cc[41]. At ~3000 atm the number density for liquid Helium is ~6.0×10^{22} #/cc.[42]

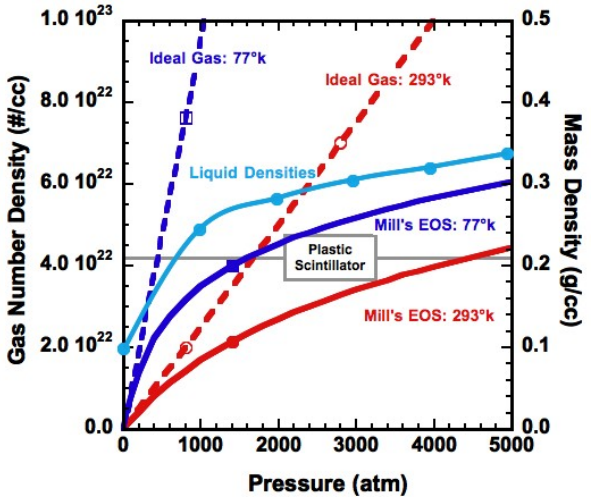

Figure 20. Helium 3 Density verse Pressure Plot. The hydrogen number density in plastic scintillator is also indicated

Note that since ^{3}He is only represents a small fraction (5.24×10^{-4}) of the natural abundance of Helium, which is primarily ^{4}He, it can be relatively expensive to obtain. The cost in quantities of hundreds of liters is ~$140/liter. Thus a detector system using a volume of 1 liter at 2000 atm of pressure would cost $280,000 in the ^{3}He costs alone!

2.5 Modeling of high-pressure capillaries.

The actual energy deposition from neutrons interacting with the gas inside a capillary array considering the differential reaction cross-sections, the angular dependence for the emission of the reaction products, the actual geometric positions for the interactions and the capillary walls and the energy deposition

due to the trajectories of the reaction products which terminate in the gas volume or the walls of the capillary requires a complex calculation. Borrowing from another work in progress, Martin and Derzon[43] have 'analytically' modeled this energy deposition for a single capillary and compared them to experimental data. A benchmark for their model was established by comparing their simulation against simulations and data presented in a paper by Shalev[44]. The results for this benchmark calculation are shown in Figure 21, which modeled thermal neutrons incident on a 2.54 cm diameter, 15.24 cm long cylinder filled with 2 atm of Krypton and 4 atm of ^{3}He. This figure, shows the probably of a given energy deposition in the gas, i.e. the probability density function (pdf) as a function of energy deposition for thermal neutrons. The good agreement between the present simulation, shown in blue, and the previous simulation and experimental data validates the present simulations.

The model was then used to calculate the energy deposition for a high pressure capillary such as are being considered for this effort. In this case 2 MeV neutrons are incident on a 150 um diameter capillary array that is considered infinitely long and filled with 2000 atm of ^{3}He and 41 atm of Xenon. The Xenon is added to increase the stopping power of the reaction products within the gas volume of the capillary and hence increase the energy deposition. The calculated spectra for the energy deposited in the gas volume for each interacting 2 MeV neutron both parallel and perpendicularly to the axis of the capillary are shown in Figure 22. As can be seen in this figure, the full energy peak is prevalent in the spectrum accounting for ~40% of the total events. The rest of the broad continuum to the lower side of the full energy peak is due to reaction products depositing energy into the walls of the capillary, i.e. the wall losses. Note the difference in the calculated spectrum calculated spectrum in Figure 22 and the spectrum in Figure 4 is that the spectrum in Figure 22 includes only the inelastic ^{3}He(n,p)^{3}H reaction and wall losses, while the spectrum in Figure 4 includes the elastic ^{3}He(n,n') recoil interaction as well as the inelastic ^{3}He(n,p)^{3}H for both the primary 2 MeV neutron as well as the inevitable Epithermal peak due to low energy neutrons which scatter into the detector but does not include the wall losses.

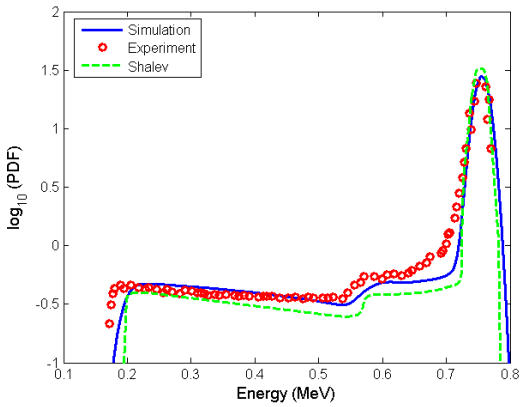

Figure 21. Comparison of thermal neutron spectral calculations and data. Martin & Derzon model (solid line); Shalev *et al*. model (dotted line), Experimental data (circles).

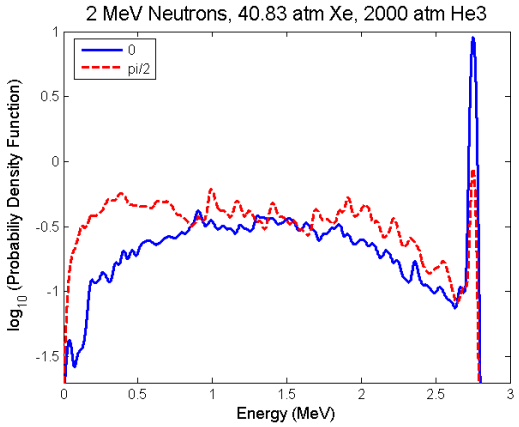

Figure 22. Calculated Energy Spectrum from a high pressure, infinite long cylinder for 2 MeV neutrons along and perpendicular to the cylinder axis.

2.6 Detection Modalities

2.6.1 Charge Collection

In gases, when charge collection is the main method for obtaining information on ionizing radiation, a number of competing mechanisms govern the detection resolution and efficiency. Briefly these are charge transfer, recombination, diffusion, fluorescence/phosphorescence/scintillation. In a charge collection system minimizing parasitic charge absorption and recombination maximizes the number of signal carriers collected. The processes governing ion and electron mobility's however affect pulse characterization through the timing and efficiency of the collection processes. One of the advantages of using charge collection is the capability for very high collections efficiencies. For air-filled parallel plate ionization chambers, with a 3.1 mm electrode separation, ion collection efficiencies of 95-99% have been reported although due to electron attachment in oxygen the fast electron collection efficiency saturated at ~70%.[45] For the noble gases the electron attachment coefficients are very small and so for our helium/xenon ion chambers the electron collection efficiency is expected to be very high.

However, as Knoll points out, electron charge diffusion is still taking place even in the presence of the electric field used for charge collection of the ion-pairs produced. Knoll quotes typical electron diffusion lengths of ~1 mm over cm lengths in ionization chambers at atmospheric pressure with electric fields of 10 kV/m.[46] This can seriously affect the charge collection efficiency in the small diameter capillary arrays we are planning on using. The standard deviation of the distance traveled by electron diffusion, σ, perpendicular to an electric field, E, over a distance x along the electric field, is given by Palladino and Sadoulet[47] as:

Equation 2.10

$$\sigma = \sqrt{\frac{2\varepsilon_k}{eE}x}$$

Where ε_k is a characteristic energy parameter directly related to the diffusion coefficient and which can be shown to be directly proportional to the collision length, l_e. Since the collision length, l_e, is inversely proportional to the number density, N_d, the standard deviation of the diffusion distance traveled is proportional to:

Equation 2.11

$$\sigma \propto \sqrt{\frac{x}{N_d}}$$

Since the number density for a high-pressure cell at 2000 atm is ~1000 times higher then at one atm, electron diffusion should be ~30 times less then Knolls value or ~30 um for a one cm long cell or ~70 um in a 5 cm long cell. If the collection electrodes are at the ends of our 5 cm long, few hundred micron diameter capillary arrays these diffusion distances could lead to ~a 10% reduction in the collected charge based on simple area arguments. Alternatively if the electrodes can be placed along the sides of the capillaries, which may add to the fabrication complexity, then this effect should be significantly reduced. This is an area that will need to be studied further in future work.

A brief description of the charge collection processes with a comparative discussion is warranted. Particle drift velocities, *v*, in gases can be estimated from:

Equation 2.12

$$v = \mu\frac{\xi}{P}$$

Where μ is particle mobility, ξ is the electric field strength and P is the pressure. From a pulse shape perspective the time collection characteristic is given by:

Equation 2.13

$$t = d / v$$

The collection time is thus given by the distance a charge has to travel divided by the drift velocity. In fact Knoll demonstrates that the rise-time for a signal in a parallel plate ion-chamber is just given by Equation 2.13 using the electron drift velocity[48]. Electron velocities in high-pressure gas (Xe, He, H) mixtures can be found in the literature. Bolitnikov[49] reports saturated electron drift velocities of 10^5-10^6cm/s at voltages of 2-5x10^3 V/cm in Xenon and Xenon/Hydrogen mixtures at 0.6 g/cm^3. Kobayashi[50] reports the saturated drift velocities of He as 2-4x10^5 cm/s at reduced electric field strengths (Electric-field / Number density) from 2-4x10^{-18} V-cm for a Xe (20 atm)-He (3 atm) gas mixture of greater than 3x10^5cm/s at reduced electric fields from 2-5x10^{-18} Vcm^2. For our high pressure He gas cell operated at ~2000 atm or at a number density of 2x10^{22} at room temperature, the signal rise-time using a 5 cm long capillary operated at the saturated drift velocity for electrons would be ~20 us, a very long time! It would also require an electric field of 400 keV over the 5 cm length to reach the saturated electron velocity. For electrode structures along the small diameter capillary the rise-times can be of order 100 ns for 300 um diameter capillaries. This would only require an electric field of 2.4 kV across the capillary but it is still slow compared with typically ICF time-scales.

Characteristic ion mobility's can be found in Piscitelli or mixtures of Xenon and Neon[51]. The reduced ion mobility's (the mobility times the number density) are 2-10x10^{21}/(m-s-V) which yields ion drift velocities of 10^2 to 10^3cm/s. The key feature is that collection times for ions is typically longer than for electrons by roughly two orders of magnitude. For 100-1000 micron drift distances the electron drift time could be expected to be 10 to 100 ns. Impurities such as H or He can affect the velocities by factors of 2-5 increasing the mobility Xenon for instance. This yields an impulse response for these systems that is inherently slow compared with typically ICF time-scales, but for time-integrated neutron diagnostic measurements such as neutron imaging or yield these represent acceptable response times. In addition if the collection time of the electronics can be set to be much shorter then the ion collection time the signal response will be set by the electron drift velocities.

The rise-time of these systems can be quite fast as inferred from the extremely fast timing accuracy of 50 ps demonstrated in resistive plate gas detectors.[52] If the actual rise-times for these detectors can be demonstrated to be of this order then direct electrical collection for neutron bang-time and neutron burn-width measurements should be feasible by deconvolving what would be effectively a step function response for the detector. In fact for this detector system they show a current pulse with a 6 ns fwhm collected in a gas cell with a 300 um electrode separations. Thus significantly enhanced performance over what we have quoted above seems possible.

Energy deposition by high energy, MeV, charged particles into Helium and Xenon gas and gas mixtures can lead to a large number of electron-ion pairs leading to high efficiencies for measuring primary particle interactions with the gas cell and for single particle counting measurement high energy resolution measurement. Dmitrenko[53] quotes W=15.6 eV as the energy to produce an ion-pair in pure liquid Xenon. For gaseous Xenon he quotes W=21.9 eV. For Helium the energy

to produce an ion-pair is given in Birk as 42.3 eV.[54] Fano factors of F=0.41 have been estimated by Doke[55], however the expected resolutions due to statistical limits alone have not been measured. A spectral resolution of 1.3% FWHM for 1 MeV gamma's has however been measured by Dmitrenko.

These charges can be collected in ionization mode (no gain) or proportional mode (electric field induced gain). Proportional mode operation, with a high electric field region, can be expected to enhance the signal strength at the cost of energy resolution and timing information.

Difficult tradeoffs in system design for electronic readout include the fact that the noise in the electronics for ionization chambers requires greater finesse then in proportional counter systems. This is due to the fact that capacitance coupling and noise issues are more difficult to handle in ionization counter systems compared to proportional counter systems. The statistical effect of the Fano factor and gain are important in the ultimate system performance. The statistical effect of the Fano factor, and gain are important in ultimate system performance. Ionization chambers (no gain) can also be much faster than proportional systems for particle drift into the proportional region is not required.

2.6.2 Scintillation Detection

In a ^{3}He detector neutrons can also be detected by observing the scintillation light created. This has the advantage of using readily available imaging and non-imaging photo-detectors as well as allowing for relatively fast response times. For Helium the mean wavelength of the fluorescence appears in the UV. Birks reports on measurements of the Helium fluorescence where the mean wavelength of observation was at 390 nm as defined with the aid of filters.[56] This value however appears to be at much longer wavelength then would be indicated by Tanaka et. al. where the Helium emission spectrum appears at much shorter wavelengths which appear in a broad continuum between 60 and 100 nm with two broad spectral peaks at 70 and 80 nm when excited by an electrical discharge.[57] However the emission spectrum appears to depend fairly sensitivity on the excitation conditions where Huffman et. al. found in addition to the broad continuum between 60 and 100 nm another broad continuum between 100 and 400 nm if he used another excitation condition.[58] We have not seen papers on the scintillation spectrum from very high pressure Helium detectors such as the ones we are considering at up to 2000 atm, but liquid Helium scintillation has been studied and they also show a broad continuum emission spectrum between 60 and 100 nm.[59]

A measure of the efficiency is given by the number of photons created, above 200 nm, per 4.7 MeV Alpha particles, which is given as 1,100. This is only ~3% of the value listed for NaI(Tl).[60]

The energy resolution a high-pressure gas scintillation spectrometer, (~14 atm ^{3}He and 14 atm Xe) to 2.5 MeV neutrons was demonstrated by Derzon[61] to be 4%. Evans demonstrated a system capable of 10% resolution for 2.5 MeV neutrons in a higher pressure, ~200 atm simple scintillator system[62]. Neutron spectra are obtained directly and discussed in more detail in the thesis by Derzon[63].

In order to effectively transport and measure this scintillation light wavelength shifting of these VUV photons into visible is typically used. Nitrogen gas can be used as a dopant for this purpose although it apparently always acts as a quenching agent and it's practical

result appears to decrease the absolute scintillation efficiency.[64] Organic wavelength shifters coated on the surface of the capillary arrays can also be used. P-quaterphenyl and p-terphenyl were used by Derzon.[65] These wavelength shifters converted the photon spectrum from the VUV into the near-UV and visible range, from 220-420 nm, and estimates of the quantum efficiencies for the conversion were 60% and 80-100% respectively. Tetraphenyl butadiene (TPB) doped polystyrene has also been used to shift the VUV scintillation light from liquid Helium to the blue with a peak wavelength of 440 nm and with a quantum efficiency of 40%.[66] It appears that wavelength shifting of the photons will be very important to transmitting the photons in these high aspect ratio capillary arrays and therefore the technology to coat the insides of the arrays is going to be critical to this detection modality.

The time response requirements for these systems depend upon their application. With regards to neutron detection for ICF applications these include neutron imaging, which requires only 10's of ns timing resolution for gating out undesired backgrounds and isolating neutrons with energies of interest, as well as neutron time-of-flight which requires a few ns response time, as well as neutron bang-time and burn width measurements which requires sub-nanosecond impulse responses and/or signals with very fast rise-times, less then 0.05 ns. To date it appears that these systems, which are typically used for photon counting spectroscopy measurements, have only been experimentally studied with bandwidth-limited systems. These systems have demonstrated rise times better than the 1 ns rise captured by a Texas Instruments 1 GHz oscilloscope with fall times of nominally 50 ns when p-terphenyl wavelength shifters were used. The time dependence of liquid-helium fluorescence was measured by Mckinsey et. al.[67] although also with a very bandwidth limited recording system. They demonstrated a rise-time better then two ns and a fall-time better then 7 ns. These response times are consistent with requirements for neutron imaging however for ICF applications requiring fast timing, such as neutron burn time measurement the actual response time for the scintillator needs to be known much better then this. Plastic scintillators used previously for these measurements have ~20 ps rise-times.[68] Thus for future work with regards to these systems significantly improved time-response measurements of the scintillator light output will be required.

One of the issues with scintillation detection is the efficiency with which the light generated in the capillary arrays can be transported out of the capillaries to a detector. The two effects of interested are the self-absorption of the scintillation light in the gas medium and the second and most important effect are the light losses due to the interaction of the scintillation light with the capillary walls.

In a long narrow capillary, such as we are proposing to use to contain the high pressure gas, one can view the capillary as a light guide with an index of refraction for the scintillation light in the gas medium, n_g, and in the capillary wall, n_w. For typical glass wall materials the index of refraction, n_w, is ~1.5. For Helium, n_g, at 2000 atm and 20°C the index of refraction can be calculated from the data in Cuthbertson's paper[69] and is ~1.025 from 190-460 nm. Xenon doping at the 10% atomic level increases the index of refraction in this photon range up to ~1.1. Unfortunately to get efficient transport of the scintillation light out of the capillaries using total internal reflection as in standard fiber-optics the cladding material, which is on the outside of a core material containing the photons to be transported, needs to have an index or

refraction which is higher then the core. The fractional solid angle for the light collection towards one end of such a stepped fiber is derived in Knoll's[70] as is given as:

Equation 2.14

$$F = \frac{1}{2}\left(1 - \frac{n_1}{n_0}\right)$$

Where n_1 is the index of refraction of the cladding material and n_0 is the index of refraction of the core material. For our case the gas filled capillary's represent the core and have an index of ~1. The glass or ceramic wall material in our capillary arrays have an index of ~1.5. Thus we cannot use total internal reflection to transport our photons out of the fibers. This is in contrast to typically scintillating fiber arrays used in ICF neutron imaging applications[71] where plastic scintillating fiber arrays, Bicron BCF-20, have been used with n_1 and n_0 values of 1.60 and 1.49 respectively, yielding a solid angle fraction of only 3%. Glass capillaries containing liquid scintillator materials have also been used where the n_1 and n_0 values are 1.49 and 1.58 respectively leading to a factional solid angle of only 3% also.[72] Thus the collection efficiency is not very high in these systems yet they are the state of the art when it comes to neutron imaging applications. It is interesting to note that for gamma-ray detection using liquid Xenon the index of refraction at the peak of it's fluorescence at 178 nm is 1.56[73] and so internal reflection could be used to transport the fundamental, unshifted fluorescence to the end of the capillaries with similar efficiencies to those quoted for the scintillating fibers.

Without internal reflection to support the transport of the photons in the detectors the collection efficiency relying just on internal reflection at the capillary interface is very small. For example for a 5 cm long glass capillary with a 50 um diameter core with core index of 1 and a cladding index of 1.5 the collection efficiency as limited by the light loss due to the reflection interface losses is only ~0.006%! For a 200 um core diameter the collection efficiency improved to ~0.03% or one-hundredth the efficiency of the plastic scintillator based systems. Without improving this result any gain made by increasing the number of scintillation photons by a factor of 10 would be more then lost due to these reflection losses.

Three technologies exist which may be able to be applied to this problem: 1) Super reflective coatings fabricated on the inside of the capillaries, 2) Bragg fiber reflection, 3) Photonic Bandgap reflection.

Mirror coating technologies have been developed for flat mirrors which increase the reflectivity of surfaces from simple aluminum coating from ~90% to over 99.5%. For instance Newport sells BroadBand Dielectric SuperMirrors which have a 99.9% reflectivity for both polarizations for angles of incidence up to 45° and at wavelength from 485-700 nm. This wavelength range is a little longer then what is required, but if the technology could be improved and coated inside our capillary arrays then the efficiency due to reflection losses would go from 0.005% for a 90% reflective coating, to 0.5% for a 99% reflection coefficient, to ~18% for a 99.9% reflection coefficient, a six times improvement over the scintillating fiber technology! We are not aware of commercial capillary arrays that are coated in this fashion but a number of coating technologies exist which may be applicable. Matsuura et. al. coated the inside of a 530 um glass capillary, 30 cm long with a 0.3 um thick nickel coatings using electroless coating techniques to generate capillaries capable of transporting soft x-rays.[74] They indicate in this paper that they are developing multilayer coatings for the inside of capillaries. This technology may

be useful for our application also. Wang et. al utilize a silver mirror reaction technique to coat silver inside of a 700 um diameter glass capillary tube 20 cm long and then formed a thin polymer film over the silver using a dynamic liquid-phase-coating procedure.[75] This effort is to optimize the laser power delivered for medical applications but these techniques could possibly be applied to coating the inside of capillary arrays with highly reflective coatings. Yet another technique for depositing coatings conformal in high aspect ratio coatings, such as capillary arrays, is atomic layer deposition techniques. A conformal coating of Cobalt up to 12 nm thick was demonstrated inside of a 20 um inside diameter glass tube 4.4 mm long.[76]

Another technique that can be used for light guiding in hollow core fibers is to use Bragg fiber reflection. In this case either single or multiple dielectric layers confine light into the hollow core fiber. Temelkuran, et. al demonstrated a Hollow core Bragg Fiber fabrication technique using rolling and drawing yielding a 25 cm long, ~200 um I.D. fiber with peak transmission at a wavelength of ~780 nm.[77] Pone, et. Al. demonstrated a technique for drawing hollow core polymer Bragg fibers for transmission of infrared photons.[78] Again we are not aware of the demonstration of fibers in the UV region for our application or the ability to form coherent bundles with these air Core Bragg fibers and technology development will be required.

Yet another possible technique for transporting the visible light out of our capillary arrays is to use photonic crystal fiber technologies where the central air core in the fiber is surrounded by a series of air holes in the cladding structure. Smith et. al. demonstrated air-core photonic crystal fibers produced using the stack and draw method which efficiently transported 1500 nm light over 100 meters in a fiber with a 12.7 um inside diameter.[79] In fact commercially available air-core photonic crystal fibers are available through Newport Corporation where single fibers capable of transmitting 470 nm light efficiently can be purchased but with an inside diameter of only 20 um and with only a small Numerical Aperture (0.051) yielding a collection solid angle fraction of only 0.07%. Whether or not this technology can be scaled up to our requirements for a fiber with an inside diameter ~10x larger and a much larger numerical aperture needs to be investigated.

If one of these photon transport schemes can be developed further then robust neutron imaging applications using scintillation light may be developed as an alternate scheme to direct charge collection. This has the advantage of using existing technology that is already being applied to neutron imaging in the ICF community. As indicated earlier the development of charge collection techniques over long aspect ratio capillaries is also a development project and so the efficient collection of the signal carriers is an critical research area for the continuation of this effort.

2.7 Fabrication and Testing Technologies

Testing of these devices requires a number of components. Figure 23 shows the components required to make the necessary measurements on a prototypical device for either optical or electrical sensing. Clean gas needs to be supplied to the devices, in this case called device primitives. A known radiation source is required for testing and calibration and pulse forming and counting electronics and/or optical recording systems are required.

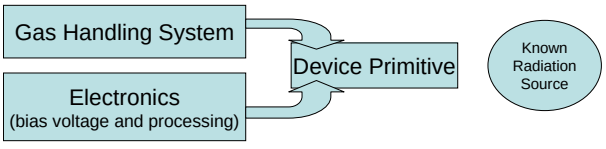

Block Components

Figure 23 Necessary components to test prototypical devices.

2.7.1 Gas Handling System

One of the most common problems in any of these gas filled systems is gas purity. As already mentioned gas mixtures affect charge mobility and pulse shape. Very low levels of impurities can also affect parasitic charge absorption and this can affect both the timing and resolution of the detector. In Derzon's, thesis, great pains were incurred to provide clean gas handling and mixing. In the thesis details were given discussing how the gas was provided. Thankfully, we do not need to reproduce the learning – only the hardware.

To provide clean gas for upcoming proof-of-principle experiments a gas manifold is being built with passivated and electropolished components where possible. Figure 24 shows a current drawing of the system. The vacuum pump out will be to the left in the figure and is not shown. A turbo pump with oil-free roughing system and a residual gas analyzer will be used as system monitor. Fill gas will be provided on bottles (not shown) on the left hand side spigots. Gas will be cleaned and mixed into bottles (not shown) using the left side spigots. After mixing, high-pressure gas from the clean gas reservoir will be supplied to the devices off the right hand spigot. Pumping will be provided at both the left and right sections separately to ensure clean gas and separate pumping to the device to maintain cleanliness. Pressure burst disks and other fittings required for vacuum safety are not shown.

Error!

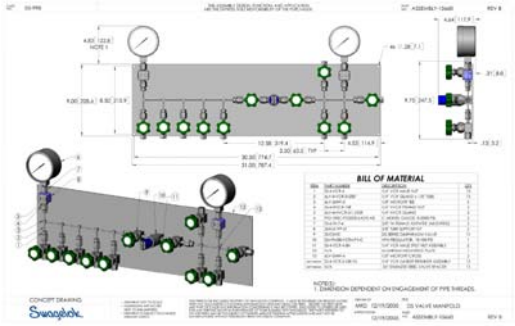

Figure 24 Gas Handling manifold.

For cleanliness metal-to-metal seals and all metal valves and pressure burst disks are used. The manifold will be checked with a residual gas analyzer for air infiltration, baked, and purged with hot Xe gas for cleanliness. Valves are provided, and provision made for including a Ti-getter system if additional cleanliness is proven necessary. A Ti-getter can be added if required.

2.7.2 Capillary Fabrication

There are at least three capillary fabrication technologies that show promise. Each has its own advantages and disadvantages.

The lowest cost and least difficult technology to test are individual capillaries made from glass capillaries. (Ron Renzi, Dave Zanini and Blake Simmons are providing this capability). These are the components that have already been successfully pressure tested to 40,000-50,00 psi. Conceptually, the prototype would look like that shown in Figure 25. This system consists of high-pressure capillaries in a one-dimensional array with nominally 10 parallel channels with electrodes at each end for electrical readout. Voltage and signal processing for these device primitives can be supplied in ion chamber or proportional counter mode. If resources permit we will wavelength shift light within the capillaries and attempt an optical readout through the

optical readout through the walls with time integrated CCDs. Depending on the results we could then request resources for time-resolved detection.

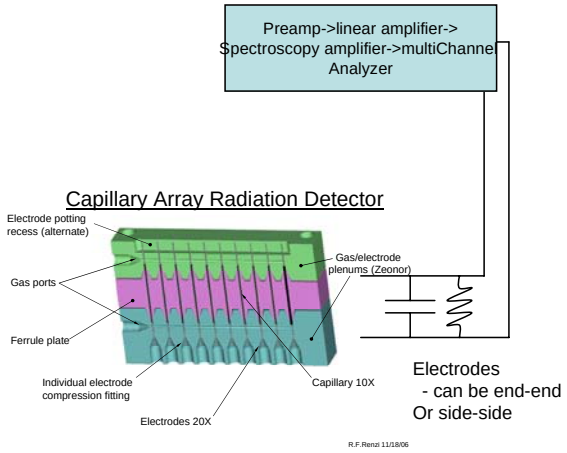

Figure 25. Prototype system for testing a 1D capillary array

An actual prototype detector system that was fabricated based on this concept is shown in Figure 26. It contains 10 5 mm long glass capillaries with 700 um outside diameters and 300 um inside diameters. The High voltage electrical leads for biasing and readout are the white cables shown in this figure. This system was hydrostatically tested to 6000 psi or ~400 atms.

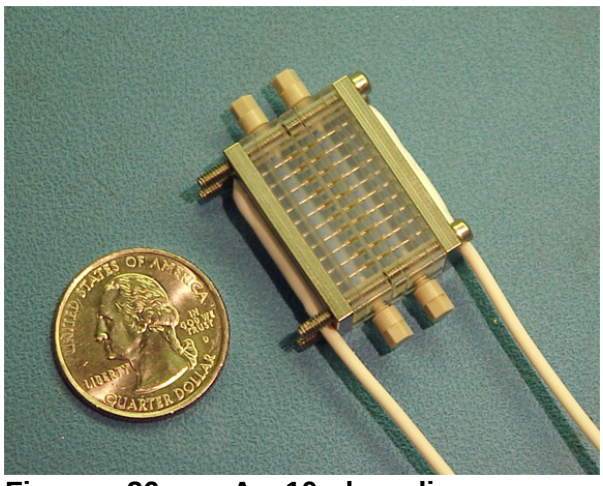

Figure 26. A 10-plex linear array containing 5 mm long glass capillaries.

A close up view of the device used in the early single capillary pressure tests is shown in Figure 27. These capillaries were 250 um outer diameter with 160 um inner diameter. They were tested with a pure He fill up to a pressure over 40,000 psi. Three capillaries were tested without any failures.

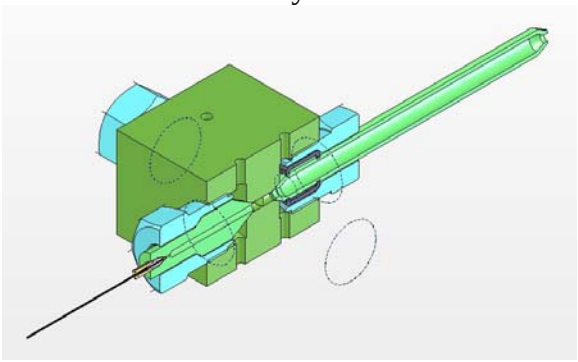

Figure 27. Single capillary test fixture. He gas was pumped into the fine capillary (on the left) thru a fill-tube to the right

Sophisticated electrode designs, such as Frisch grid analogues can be used to improve resolution if required. The need for resolution is very dependent upon application and in our early experiments we are only interested in detecting signal amplitude and showing proof-of-principle.

This method has the advantage of being the most straightforward to test and prototype multiple configurations and it is the lowest cost. The drawback is that we have not yet developed credible concepts for mass production of thousands of capillaries in a system.

The next most expensive option to test is the LTCC (Low-temperature Co-Fired Ceramic) option. In this technology wafers can be made, electrodes provided and high pressure can be contained. Five thousand psi has been contained in LTCC devices although not under our required conditions.

Modification of this technology to our requirements for massively parallel capillaries is straightforward. Fabrication is lithographic and lends itself well to mass production.

Dimensions can be as small as 100 microns or as large as a centimeter. Complex geometries can be fabricated with this technique.

The SNL MESA program has developed a number of methods by which the structures desired could be made using the 6 in. silicon wafers used in the Materials Development Lab (MDL) and the new microfab facilities.

For this technology we envision fabrication on standard 6 inch Silicon wafers of nominally 0.7 mm thick. The sensors patterns could be made as horizontal lay downs into a six-inch wafer with a 1 cm^2 individual channel. This pattern can be placed multiple times over the wafer and a signal-processing chip capable of handling the nominal 180 capillaries/wafer. Low noise and high-energy resolution should be possible in this configuration.

In Figure 28 we show a cross section view of the fabrication that can be done in these silicon devices. Buried traces can be laid into the silicon and channels etched for the gas paths. Strength calculations have been performed for devices fabricated in silicon that indicate that pressures can be contained up to ~1200 atm in capillaries which are 70 um diameter with a 150 um center-to-center spacing.[80] If higher pressures are required, as we have proposed for fast neutron detection, additional robust support can be given to the capillaries. The highest risk feature is the packaging required to adapt the gas-fill line and mate it to the Silicon. If the Swajelok threaded fitting has problems a back up plan to use brazed fittings to an electroplated surface on the Silicon. This has been done before but not for high-pressure fittings. To perform this work we will involve the device-packaging group at SNL and perform both shock and stress relief to the wafer and external contacts.

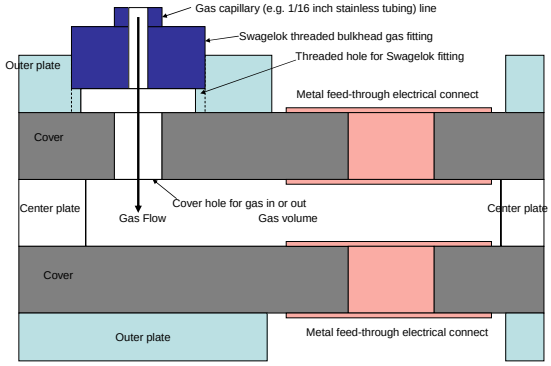

Figure 28. Side view of etched patterns and structures for gas fill, electrical readout and feedthroughs

2.8 Non-Proliferation and Homeland Defense Applications using Active WMD Detection

Active detection, meaning using a radiation source to probe an unknown sample is a known to be an incredibly powerful technique. More specifically pulsed neutron activation is a technique that is well understood and offers great diagnostic power. We illustrate this below with a short description of the state-of-the-art in this area. After that introduction we which to constrast it with what may offer numerous advantages in a system made of fast detectors (such as those we discuss in this report) when matched to a very short (10-50 ns) neutron source such as may be made in a dense plasma focus or other pulsed power system.

The RapidScan system uses a chain of short (1ns) but low yield 14 MeV neutron pulses created by an accelerator at 5 MHz to irradiate a target and then image the target. This technique allows you to scan large three dimensional objects for SNM or contraband. Technologically it provides the good current understanding of what may be present. The

Eberhardt system provides even more information. These are both presently large systems, they require expensive infrastructure, high dose to the target and a long time for interrogation and data analysis.

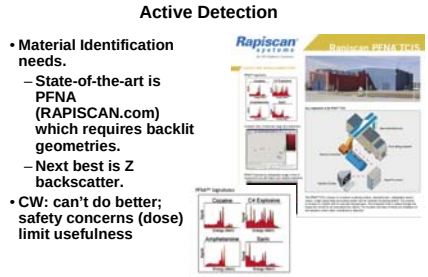

Figure 29. Information regarding pulsed neutron detection (from Rapidscan.com 5/06).

What we will claim here is that intense short neutron pulses can still provide the activation information provide by long pulses but that they also provide time-of-flight options for characterizing the target.

When Derzon started arguing for time-of-flight interrogation a few years ago it had not been done. Now, time-of-flight radiography is becoming a useful tool for small object imaging.[81, 82] These results can be extrapolated to how one might use such a system for border security or other contraband/SNM detection. An excellent review of the state of the art in contraband detection using portal systems can be found in the article by Buffler.[83] Eberhardt, et al, provides another set of insights through the combination of gamma and neutron detection.[84] In this article they discuss the characteristics of neutron and gamma diagnostics and radiography in the detection of contraband and explosives. They also discuss the value of doing these concurrently. Comparisons are also made between the Ancore Corporation technology (using the PFNA pulsed source) with 50 mm diameter plastic scintillators for readout.

It is the opinion of the authors, made many times over the last few years that Sandia is sitting on the best set of technologies of all of these for fulfilling this particular mission. As a critical national security issue SNL could potentially combine its pulsed power sources with detector technologies and MESA capabilities to create systems that far outperform those referenced here.

The pulsed power technology can result in high ($>>10^8$ neutrons/pulse) in single pulses as well as intense gamma bursts. Using the time-of-flight information present in the intense bursts would allow more information to be captured as well as lower dose to the object. Sandia is better prepared to fill this need than anywhere else but as the literature shows the community is moving in this direction – the question here is whether SNL wishes to be a part of the solution.

In this case we'd envision a pulsed power driver creating impulses of neutrons (and gammas) for time-of-flight unfolding. A system may consist of a point radiation source (for example a dense plasma focus driver) coupled to either a large area detector, such as in Rapid-Scan or potentially a few widely spaced point detectors. Figure 30 illustrates such a detection system. Source to object distances and object to detector distances of ~3 meters are envisioned for objects of a nominal size of three meters by six meters.

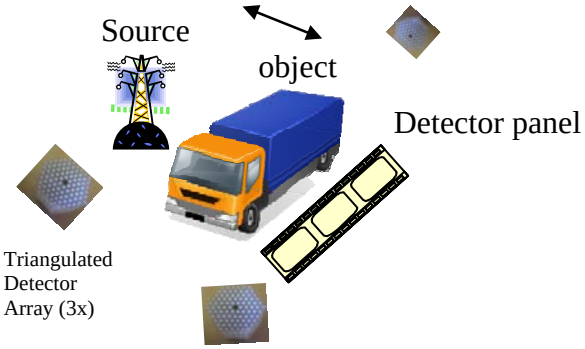

Figure 30. Representation of pulsed detection system.

For such a configuration a source brightness of 10^{10} neutrons would give an unscattered flux of $2.5x10^3$ n/cm^2. The implication is that a 1 mm^2 pixel of 10% efficiency has a 2.5% chance of detecting an unscattered neutron and a low chance of detecting two, which is what you want. This is a good match for doing single particle detection and of estimating the direct attenuation. With a large panel detector there are large number of neutrons for high-resolution direct imaging ~10^5 n/m^2. At a pixel resolution of 1 mm^2/pixel, and a panel of size 10 m^2 that same source will provide nominally 10^6 neutrons in both the direct and scattered fluxes. This may provide enough signal for a single pulse to generate both clear forward images and scattered images and TOF spectra.

Individual pixels detecting the indirect or scattered flux have additional information as well. . This is similar to what a short-pulsed neutron interrogation for portal inspection would give. For example we compare estimates by Meade for NTOF signal backgrounds on the NIF due to neutron interactions with the chamber wall and which are shown in Figure 31.[85] In this case the neutron-scattered contribution is seen to be down in intensity by 10^3 of the peak.

QuickTime™ and a
TIFF (Uncompressed) decompressor
are needed to see this picture.

Figure 31. Comparison of three TOF spectra: (1) neutrons arriving directly from the target (the signal), compared with background produced when the target neutrons scatter from the walls of the NIF chamber, producing lower-energy, backscattered (2) neutrons, and (3) gamma rays.

For instance, in the ICF programs' diagnostic development THz time-resolved neutron spectroscopy has been performed.[86, 87] The scattered information is even more valuable however than the direct. Here the signal per unit time is down by 3- to 4- orders of magnitude however microseconds are available and the time-of-flight information provides spatial accuracy of nominally 1 cm for 14 MeV neutrons. The scattered radiation creates a 3D kernal or point spread function for the location of material based on both the density and Z of the material present in the object.

The pulse power program has generated short (<100ns) pulses of up to 10^{12} neutrons, it has created continuous operation sources of khZ and has lately created laboratory sized devices capable of driving 100 KJ targets. This implies that a relatively small sized nominal one million dollar per unit pulsed power driver may be obtainable (estimate given by M. Buttram).

3 CONCLUSIONS AND FUTURE DEVELOPMENTS

This work has taken a critical look at the potential benefits and future work primarily required to develop high-pressure helium gas detectors for fast neutron, ~1-15 MeV, ICF applications. These innovative high pressure Helium detectors are made possible by utilizing Sandia's expertise in Micro-electrical Mechanical fluidic systems, and appear to have many beneficial performance characteristics with regards to making these neutron measurements in the high bremsstrahlung and electrical noise environments found in High Energy Density Physics experiments and especially on the very high noise environment generated on the fast pulsed power experiments performed here at Sandia. This same system may dramatically improve active WMD and contraband detection as well when employed with ultrafast (10-50 ns) pulsed neutron sources. Specifically we add preliminary suggestions for active detection, which would couple this style of detector with a short-pulsed neutron source such as that which could be made with a pulsed power driver (e.g. a dense plasma focus). In this work we borrow heavily from and contribute to on-going work on a pixilated ^{3}He-system for thermal neutron detection.[1]

The relative benefits for using ^{3}He verse ^{4}He and Xenon-doped Helium were presented indicating that for fast neutron detection ^{4}He was a very viable and low cost choice as compared with ^{3}He if a factor of two in energy deposition for DD neutrons and 50% less energy deposition for DT neutrons was acceptable. Xenon doping of the Helium improves the number of scintillation photons by a factor of 10 and shifts the scintillation photon energy from the UV towards longer wavelength improving the detectors collection and detection efficiency. The price for this was an increase in the high-energy bremsstrahlung sensitivity, but this may be acceptable depending on the application. Wavelength shifters, either, a nitrogen gas dopant or organic flour coatings such as tetraphenyl butadiene (TPB) or P-terphenyl can also be used to further improve the collection and detection efficiency of the system. Alternatively viewing the ion-pairs produced directly using charge collection removes the need for Xenon doping as the number of ion-pairs created is not very dependant on the doping and is comparable in number to the quantity of scintillation photons generated in the Xenon-doped Helium. In both cases the collection efficiency of ion-pairs or scintillation light in the long aspect ratio channels proposed is a concern and will require further investigation as indicated below. However charge collection could be very efficient and with a high enough time response that ICF neutron imaging applications should be very accessible.

A comparison with standard fast neutron detectors using plastic scintillators was performed and indicated that in this neutron energy regime high pressure, 2000 atm, gas detectors at room temperature would have similar interaction distances while the gas scintillator systems can generate nearly 10 times the number of signal carriers with a significantly lower sensitivity to bremsstrahlung photons yielding figures of merit that can be ~50 times higher then for standard scintillators. Signal to noise improvements in the detected signal for imaging applications were shown to be improved by up to a factor of two over plastic scintillator based systems if the signal carriers could be collected with similar efficiencies. Using these high-pressure gas systems at liquid nitrogen temperatures further improves their efficiency by doubling the number of gas atoms and yielding a signal to noise ratio

improvement of 20% due to primary neutron interactions compared with plastic scintillators.

In addition to the larger number of signal carriers generated and the lower bremsstrahlung sensitivity the reaction product ranges for high pressure Helium were shown to have ranges which may yield a factor of four to eight improvement in the spatial resolution of the detector as compared with plastic scintillator detectors presently used! This can have a significant impact on the design specifications for an imaging detector for ICF applications.

The viability for these detectors to allow for improved neutron detection, especially in high bremsstrahlung environments for neutron imaging, neutron time of flight, neutron bang and burn width measurements looks very encouraging, however future work needs to address a number of issues.

The effect of the capillary array structure on the bremsstrahlung noise characteristics of the detector needs to be considered. Detailed Monte-Carlo calculations can be done and prototype detectors can be tested in high bremsstrahlung environments such as Sandia's GIF and the HERMES and Z-accelerator facilities. Monte-Carlo calculations and tests on prototype systems need to be performed to verify the spatial resolution characteristics of these high-pressure Helium capillary array systems.

In the area of detection modalities utilizing charge collection the effect of electron diffusion limiting the charge collection efficiencies in the long narrow capillaries that we envision utilizing needs to be studied through modeling and experiments to define electrode structures and fabrication techniques that will allow for a high collection efficiency. The limits on the time response for such a response for such a system also needs to be investigated to see what the limits are on the impulse response of the system and to see if sub-nanosecond rise-times can be achieved.

For optical detection of the fluorescence photons generated photon collection efficiencies in high aspect ratio capillary array structures also needs to be explored and demonstrated. As indicated in the text three techniques are possible for transporting light out of these low index gas filled cores imbedded within a high index glass or ceramic matrix. These include techniques that generate highly reflective coatings on the insides of the capillaries, greater then 99.5%, or techniques that use Bragg reflection or photonic band-gaps. These techniques have been demonstrated in single fibers and the ability to incorporate them into the fabrication of capillary arrays at the appropriate photon energies and scale sizes needs to be demonstrated. In order for these techniques to work it seems critical to be able to wavelength shift the UV scintillation photons using organic wavelength shifters into a ~400 nm wavelength band to better match to these transport technologies. This will require the development of coating technologies for these wavelength sifters that are also consistent with these long aspect ratio capillaries. In addition for applications such as for neutron burn width measurements characterization of the time-response of the scintillation light on a faster timescale then has presently been performed, on the tens of picosecond time-scale, needs to be done.

These detector systems have the potential to significantly impact neutron diagnostic systems used for ICF and for Non-Proliferation and Homeland Defense Applications. A significant amount of research remains to be accomplished but we believe the payoffs can be large.

4 REFERENCES

[1] M.S. Derzon, et. al. SAND Report SAND2007-7367C

[2] Glenn Knoll, 'Radiation Detection Measurement', John Wiley & Sons, Inc. 1989, page 485.

[3] M.B. Chadwick, P. Oblozinsky, M. Herman et al.,"ENDF/B-VII.0: Next Generation Evaluated Nuclear Data Library for Nuclear Science and Technology", Nuclear Data Sheets, vol. 107, pp. 2931-3060, 2006. Data in Plot uses JENDL3-3 cross-sections obtained from the National Nuclear Data Center website: www.nndc.bnl.gov.

[4] Glenn Knoll, 'Radiation Detection Measurement', John Wiley & Sons, Inc. 1989, page 485.

[5] S. Shalev, Z. Fishelson, and J.M. Cuttler, Nucl. Instrum. Meth. 71, 292 (1969)

[6] Glenn Knoll, 'Radiation Detection Measurement', John Wiley & Sons, Inc. 1989, page 495.

[7] Data in Plot uses JENDL3-3 cross-sections obtained from the National Nuclear Data Center website: www.nndc.bnl.gov.

[8] A. Sayres and M. Coppola, Rev. Sci. Instrum. 35, 431 (1964).

[9] J.W. Leake, Nucl. Instrum. Meth. 63, 329 (1968).

[10] K.G. Harrison, Nucl. Instum. Meth. 166, 197 (1979).

[11] L.V. East and R.B. Walton, Nucl. Instrum. Meth. 72, 161 (1969).

[12] Glenn Knoll, 'Radiation Detection Measurement', John Wiley & Sons, Inc. 1989, page 528.

[13] Pierre Marmier and Eric Sheldon, 'Physics of Nuclei and Particles', Academic Press, Inc. 1969, page 99.

[14] Photon Cross-section data is from the National Institute of Standards and Technology XCOM Photon Cross Section Database program which can be found at: http://physics.nist.gov/PhysRefData/Xcom/Text/XCOM.html.

[15] Ion particle ranges were calculated using J. F. Ziegler's SRIM2006 Particle Interaction with matter code, www.srim.org/index.htm

[16] Electron ranges were calculated using the formulas 3.3 and 3.4 in, Robley D. Evans, 'The Atomic Nucleus', McGraw-Hill Book Company 1955, page 625.

[17] T. Shima, et. Al. Physica Scripta. Vol. T104, (2003) 164.

[18] V. Yu. Glebov, et. al. Nucl. Instrum. Meth. 75, (2004) p3559.

[19] Robert E. Chrien, David F. Simmons and Dale L. Holmberg, Rev. Sci. Instrum. 63 (1992) p4886.

[20] G. L. Morgan, et. al. Rev. Sci. Instrum. 72 (2001) p865

[21] C. Stoeckl, et. al. Rev. Sci. Instrum. 74 (2003) p1713

[22] M. J. Moran, J. Koc, C. A. Barrera and E. C. Morse, Lawrence Livermore National Laboratories report, UCRL-JC-152377, (2003).

[23] Op. Cite. M.B. Chadwick, et. al.,"ENDF/B-VII.0: Next Generation Evaluated Nuclear Data Library for Nuclear Science and Technology". Data in Plot uses ENDF/B-VII.0 for Hydrogen elastic, ENDF/HE-VI for Carbon elastic; JEFF-3.1/A for Carbon inelastic and JENDL3-3 for ^{3}He cross-sections obtained from the National Nuclear Data Center website: www.nndc.bnl.gov

[24] Figure obtained from Saint-Gobain Crystals Scintillation Products Catalog: SGC_Organics_Brochure_2005.pdf.

[25] J.B. Birks, 'The Theory and Practice of Scintillation Counting', Pegamon Press, Oxford, 1964, p596.

[26] Saint-Gobain Crystals Scintillation Products Catalog: SGC_Organics_Brochure_2005.pdf.

[27] D. Ress, R. A. Lerche, R. J. Ellis, G. W. Heaton and D. E. Lehr, Rev. Sci. Instrum. 68 (1995) p4943.

[28] L. Disdier, R. A. Lerche, J. L. Bourgade, V. Yu. Glebov, Rev. Sci. Instrum. 75, (2004) p2134.
[29] M.S. Derzon, Thesis, "A He3 Filled Gas Scintillation Spectrometer for Fusion Neutron Measurements', 1987, pages 46 and 50.
[30] J.B. Birks, Op Cite, p581.
[31] Glenn Knoll, op cite, p131.
[32] L. Disdier, op. cite.
[33] Photon Cross-section data is from the National Institute of Standards and Technology XCOM Photon Cross Section Database program which can be found at: http://physics.nist.gov/PhysRefData/Xcom/Text/XCOM.html.
[34] J.B. Birks, op cite, page 599.
[35] Op. cite, www.srim.org/index.htm
[36] L. Disdier, et. al. RSI 75, page 2134, 2004.
[37] "Helium-3 and Helium-4" by William E. Keller, Plenum Press, N.Y. 1969, page 40.
[38] E.R. Grilly and R.L. Mills, Ann. Phys. 8, (1959), page 1.
[39] R. L. Mills, D.H. Liebenberg, and J.C. Bronson, Phy. Rev. B 21, 21 (1980).
[40] James D. Cramer, LANL Internal Report, 'The Compressibility of Gaseous Mixtures of Helium-Nitrogen and Helium-Deuterium at High Temperatures', LA-3250-MS (1965).
[41] W.H. Keesom, 'Helium', p207, Printed in Holland by Meijer's Boek-En Handelsdrukkerij, Wormerveer.
[42] David A. Young, A. K. McMahan and Marvin Ross, Phys. Rev. B Vol. 24, 5115 (1981).
[43] Martin and Derzon, Draft, SAND06-,
[44] S. Shalev, Z. Fishelson and J. M. Cuttler, Nucl. Instrum. Meth. 71, 292 (1969).
[45] J.W. Boag, E Hochhauser and O.A. Balk, Phys. Med. Biol. 41 (1996) p885.
[46] Knoll, op cite, p132.
[47] V. Palladino and B. Sadoulet, Nucl. Instr. And Meth. 128 (1975) 323 eq. 7.
[48] Knoll, op cite, p151.
[49] A.E. Bolinikov, et al, "properties of compressed Xe gas as the medium for High-Pressure Xe Spectrometers," Nuclear Science Symposium and Medical Imaging Conference, 1994, IEEE Conference Record Volume 1, 30 Oct.-5 Nov. 1994 Page(s):74 - 78 vol.1.
[50] S. Kobayashi,Jpn J. Appl. Phys. Vol. 42, (2003) pp. 333-334, part 1, No. 1.
[51] D. Piscitelli, et al, "ion Mobilities in Xe/Ne and other rare gas mixtures", Phys. Rev, E 68,046408 (2003).
[52] P. Fonte, et. al. Nucl. Inst. and Meth. A 449 (2000) 295.
[53] V.V. Dmitrenko, et al, Proceedings of the SPIE, Vol. 1734 Gamma-Ray Detectors (1992) p90.
[54] Birk, op. cite. P 581.
[55] T. Doke, et al, Nucl. Inst. And Meth. 134, (1976) 353.
[56] J.B. Birks, Op Cite, p595.
[57] Y. Tanaka, A. S. Jursa, and F. J. Leblanc, J. Opt. Sco. Am. 48, 304 (1958).
[58] R.E. Huffman, Y. Tanaka, and J.C. Larrabee, J. Opt. Soc. Am. 52, 851 (1962).
[59] C. M. Surko, R. e. Packard, G. J. Dick, and F. Reif, Phys. Rev. Letters 24, 657 (1970).
[60] Glen Knoll, op. cite. Table 8-4, page 247.
[61] M. S. Derzon, D. R. Slaughter, and S. G. Prussin, Rev. Sci. Instrum. **56**, 1090 (1986).
[62] A.E. Evans, Jr 'Development of a High-Pressure 3He Neutron Scintillator Spectrometer', Los Alamos Program Technical Report: LA-Q2TN-82, April 29, 1982.
[63] M.S. Derzon, Thesis, "A He3 Filled Gas Scintillation Spectrometer for Fusion Neutron Measurements', 1987.
[64] Birks, op. cite. p591.
[65] M.S. Derzon, Thesis, op. cite. p56.
[66] D.N. McKinsey, et. al. Phys. Rev. A 67, 062716, (2003).
[67] D.N. McKinsey, et. al. op. cite.
[68] R. A. Lerche and T. J. Ognibene, Rev. Sci. Instrum. 70 (1999) 1217.

[69] C. Cuthbertson and N. Cuthbertson. Proc. Roy. Soc., London, A 135, 40 1932.
[70] Glen Knoll, op. cite. Eq. 8.14, page 251.
[71] G. P. Grim, et. al. Rev. Sci. Instrum. 75, (2004) p3572.
[72] L. Disdier, R. A. Lerche, J. L. Bourgade and V. Yu. Glebov, Rev. Sci. Instrum. 75, (2004) p2134.
[73] L.M. Barkov, et. al. Nucl. Instr. And Meth. A 379 (1996) 482.
[74] Yuji Matsuura, Tadaaki Oyama, and Mitsunobu Miyagi, Appl. Opt. 44 (2005) 6193.
[75] You Wang, et. al. Appl. Opt. 36 (1997) 2886.
[76] Booyong S. Lim, Antti Rahtu and Roy G. Gordon, Nature Materials 2, (2003) 749.
[77] Burak Temelkuran, et. al. Nature 420 (2002) 650.
[78] Elio Pone, et. al. Optics Express 14 (2006) p5838
[79] Charlene M. Smith, et. al. Nature 424 (2003) p657.
[80] Op cite, Derzon et. al. SAND Report SAND2007-7367C
[81] Vartsky, D., et al. Nucl. Inst. and Meth. A 542 (2005) p206.
[82] Dangendorf, V., et al. Nucl. Inst. and Meth. A 542 (2005) p197.
[83] Buffler, A., Radiation Physics and Chemistry 71 (2004) p853.
[84] Eberhardt, J.E., et al., Applied Radiation and Isotopes 63 (2005) p179.
[85] William C. Mead, 'Assessment of Neutron and Gamma-Ray Scattering Background. in the NIF Target Chamber for a Proposed Capsule r Diagnostic', 11/16/2000, Adaptive Network Solutions Research, Inc. Los Alamos, NM (wcm@ansr.com, www.ansr.com/rpt/ansr_rpt_apr36_ph_i_av.pdf)
[86] Cable, M.D., 'Neutron spectroscopy at very high counting rates for inertial confinement fusion', Abstracts of Papers of the American Chemical Society, 193 (1987) p91.
[87] Lerche, R.A., et al., Rev. Sci. Instr. 63, (1992) p4877.

5 APPENDIX A: NEUTRON DETECTION ERROR ANALYSIS

A neutron signal is never directly observed. Instead signal carriers are generated from the neutron interacting with target nuclei via the coulomb and strong nuclear force interactions to generate recoil ions or nuclear reactions who's energy deposition can then be observed through electromagnetic interactions with the surrounding media. The secondary interactions generate signal carriers that are either electron-ion pairs or scintillation light, that can be observed by a detector system.

Thus the observed signal can be written as:

Equation 5.1

$$N_o = \varepsilon N_s N_n$$

Where:

- N_o = the total number of signal carriers observed in counts
- N_n = the number of neutrons interacting in the detector
- N_s = the number of signal carriers generated per incident neutron
- ε = the collection efficiency for the signal carriers by the detector system which will be treated as a constant

Now assuming simple Poisson counting statistics for the number of neutrons incident as well as the number of signal carriers generated we will utilize the error analysis concepts developed in the book, " Data Reduction and Error Analysis for the Physical Sciences" 3rd Edition by Philip R Bevington and D. Keith Robinson, published by McGraw-Hill Higher Education, 2003. In this text they develop the error propagation formula for the variance in a quantity that is a function of a set of variables that are uncorrelated. This is given as equation 3.14 in their text and which yields the following equation for the variance in the observe number of signal carriers:

Equation 5.2

$$\sigma_{No}^2 = \left(\frac{\partial N_o}{\partial N_s}\right)^2 \sigma_{Ns}^2 + \left(\frac{\partial N_o}{\partial N_n}\right)^2 \sigma_{Nn}^2$$

Yielding:

Equation 5.3

$$\sigma_{No}^2 = \left(\varepsilon N_n\right)^2 \sigma_{Ns}^2 + \left(\varepsilon N_s\right)^2 \sigma_{Nn}^2$$

Which yields the square of the relative error in the observed signal in terms of the sum of the square of the relative errors in the number of signal carriers generated per neutron interaction with the square of the relative error in the number of neutrons interacting with the detector.

Equation 5.4

$$\frac{\sigma_{No}^2}{N_o^2} = \frac{\sigma_{Ns}^2}{N_s^2} + \frac{\sigma_{Nn}^2}{N_n^2}$$

For Poisson statistics the signal to noise ratio is given by:

Equation 5.5

$$\left(\frac{S}{N}\right)_{Ni} = \frac{N_i}{\sigma_{Ni}} = \frac{N_i}{\sqrt{N_i}} = \sqrt{N_i}$$

Where N_i is the number of counts for any one of the variables. However as explained by Knoll[1] the observed statistics for signal carriers can be different then given by Poisson statistics, due to correlations in the formation of the signal carriers and the concept of the Fano factor has been introduced to include this difference. He defines the Fano factor as the ratio of the observed variance in the signal carriers to the variance predicted by Poisson

[1] Glenn Knoll, 'Radiation Detection Measurement', John Wiley & Sons, Inc. 1989, page l15

statistics as indicated by the following equation:

Equation 5.6

$$F = \frac{\sigma^2_{Ns\_o}}{\sigma^2_{Ns\_p}}$$

For certain proportional gases the Fano factor is seen to be between 0.05 and 0.2. F=0.05 to 0.2, (see p. 176 Knoll), significantly reducing the predicted variance. In semi-conductors it is 0.13 to 0.14. For an ion chamber or a scintillator the Fano factor can be 0.2-1. F is rarely much larger than 1.

Therefore, from equations 4, 5 and 6, we can express the signal to noise for the observed signal in terms of the counting statistics on the number of neutrons interacting in the detector and the number of signal carriers generated per neutron including the Fano factor for this process:

Equation 5.7

$$\frac{1}{\left(\frac{S}{N}\right)^2_{No}} = \frac{F\sigma^2_{Ns}}{N_s^2} + \frac{\sigma^2_{Nn}}{N_n^2}$$

Equation 5.8

$$\left(\frac{S}{N}\right)^2_{No} = \frac{N_s^2 N_n^2}{FN_n^2\sigma^2_{Ns} + N_s^2\sigma^2_{Nn}}$$

Equation 5.9

$$\left(\frac{S}{N}\right)_{No} = \frac{N_s N_n}{\sqrt{FN_n^2 N_s + N_s^2 N_n}} = \frac{\sqrt{N_s N_n}}{\sqrt{FN_n + N_s}}$$

Therefore the signal to noise of the observed detector signal depends on the counting statistics for both the primary neutrons interacting in the detector and the number of signal carriers generated and the Fano factor for the signal carrier generation. This equation indicates that for the case of F*Nn >> N_s the signal to noise of the observed S/N approaches the square root of (N_s/F). Thus for a large number of neutrons interacting with the detector the signal to noise on the observed signal improve as the square root of the number of signal carriers generated. For the case where the number of signal carriers is much greater then the Fano factor times the number of neutrons, i.e. N_s >> FN_n, the S/N approaches the square root of N_n.

This seems to be an appropriate model of the noise characteristics when looking at a signal, such as the observed signal in a pixel of a neutron imaging system.

For the case where one is interested in inferring the noise characteristics for the quantity of inferred incident neutrons then it would seem that we should look at the error analysis in the equation:

Equation 5.10

$$N_n = \frac{N_o}{N_s}$$

As shown in Bevington[2] in equation 3.25 the variance in a quantity that is found from the division of two statistical quantities where the covariance term can be neglected is the same as that for the multiplication of the two quantities.

Equation 5.11

$$\frac{\sigma^2_{Nn}}{N_n^2} = \frac{\sigma^2_{Ns}}{N_s^2} + \frac{\sigma^2_{No}}{N_o^2}$$

The signal to noise for the measured number of neutrons, including the Fano factor, yields:

[2] Philip R Bevington and D. Keith Robinson, " Data Reduction and Error Analysis for the Physical Sciences" 3rd Edition, McGraw-Hill Higher Education, 2003, p44

Equation 5.12

$$\frac{1}{\left(\frac{S}{N}\right)^2_{Nn}} = \frac{F\sigma^2_{Ns}}{N^2_s} + \frac{\sigma^2_{No}}{N^2_o}$$

Therefore the signal to noise for the inferred incident neutron flux is given as:

Equation 5.13

$$\left(\frac{S}{N}\right)^2_{Nn} = \frac{N^2_s N^2_o}{FN^2_o\sigma^2_{Ns} + N^2_s\sigma^2_{No}}$$

Given that:

Equation 5.14

$$\left(\frac{S}{N}\right)_{Nn} = \frac{N_s N_o}{\sqrt{FN^2_o N_s + N^2_s N_o}} = \frac{\sqrt{N_s N_o}}{\sqrt{FN_o + N_s}} = \frac{\sqrt{N_s N_n}}{\sqrt{FN_n + 1}}$$

Therefore if the Fano Factor times the number of interacting neutrons, N_n, is large compared with 1, then the signal to noise for the inferred observed neutrons depends on the square root of the number of signal carries divided by F. This is expected to be the case for most situations and so increasing the number of signals by a factor of 10 should improve the signal to noise in the detected neutrons by a factor of 3.

6 DISTRIBUTION

1	MS0123	Henry Westrich	1011
1	MS0959	Kenneth A. Peterson (electronic)	2452
1	MS1080	Mark S. Derzon	1749-2
1	MS1080	Paul Galambos (electronic)	1749-2
1	MS1080	Keith Ortiz (electronic)	1749-2
1	MS1196	Gordon A. Chandler	1677
1	MS1196	Ramon J. Leeper (electronic)	1677
1	MS1196	Alan Nelson (electronic)	1677
1	MS1196	Carlos Ruiz (electronic)	1677
1	MS1196	Gary Cooper (electronic)	1677
1	MS1316	Shawn B. Martin (electronic)	1415
1	MS9292	Ronald F. Renzi (electronic)	8125
1	MS0899	Technical Library (electronic)	9536
1	MS0123	D. Chavez, LDRD Office (electronic) 1011	
1	MS0161	Patent and Licensing Office (electronic) 11500	
1	MS0161	Kevin Bieg (electronic)	11500


Sandia National Laboratories